Moderní experimentální metody
Rentgenová a elektronová spektroskopie I

Spektroskopie absorpční hrany rtg záření

- Principy, experimentální realizace
- Metody: XANES, EXAFS
- Postupy vyhodnocení dat, příklady
- Magnetismus – XMCD
- RIXS

Moderní experimentální metody
Rentgenová a elektronová spektroskopie II

Anomální rtg difrakce
- Kramersovy-Kronigovy relace
- Anomální difrakce – principy, použití
- DAFS

Flurescenční spektroskopie
- Spektroskopie charakteristického záření (XRF, EDS, WDS)
- Kvalitativní a kvantitativní analýza
- TRXRF
- Fluorescence ve stojaté vlně (SW-XRF) – rtg reflexe, difrakce

Moderní experimentální metody
Rentgenová a elektronová spektroskopie III

Fotoelektronová spektroskopie

- Fotoelektronová spektroskopie (XPS) a spektroskopie Augerových elektronů (AES)
- Úhlově rozlišená fotoelektronová spektroskopie (ARPES)
- Experimentální aspekty
- Zdroje: ARPES, ARUPS
- Detektory
- Příprava vzorků

Absorpce rtg záření

Ionizace hluboké elektronové hladiny – absorpční hrana.

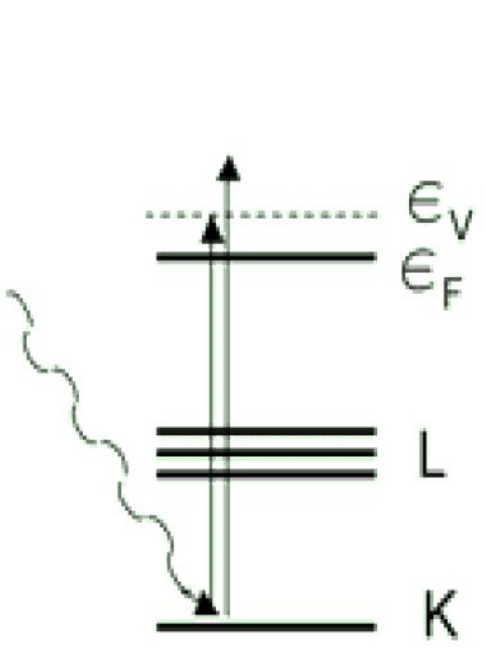

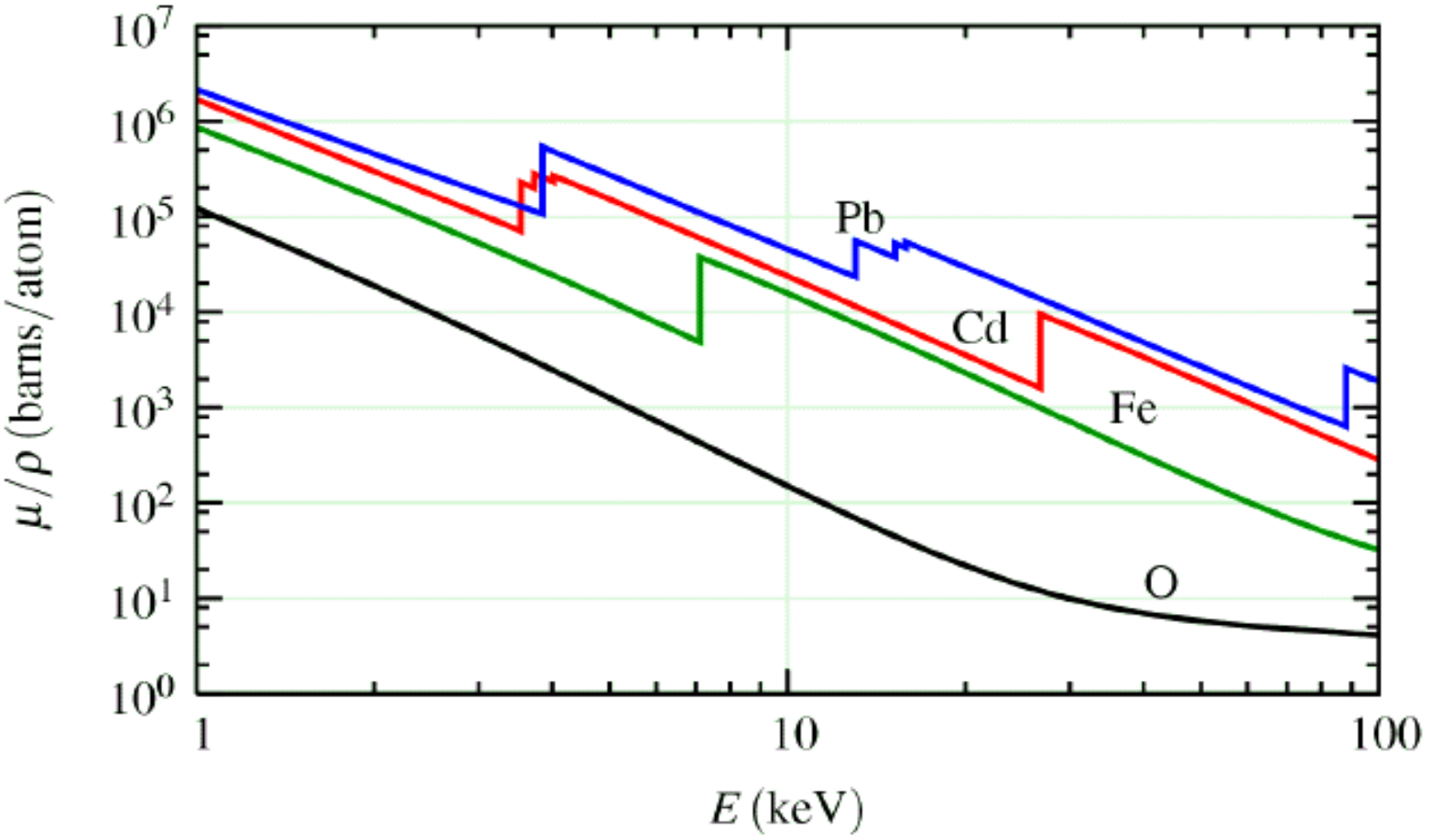

Závislost absorpce na vlnové délce pro olovo (Z=82).

Empirická závislost absorpce na energii mimo absorpční hranu:

$$\alpha(\epsilon) = \frac{a}{\epsilon^3} + \frac{b}{\epsilon^4} \ ,$$

XAFS

Rentgenová absorpční spektroskopie jemné struktury
X-ray absorption fine structure – XAFS
Extended x-ray absorption fine structure – EXAFS
Near-edge x-ray absorption fine structure – NEXAFS
X-ray absorption near-edge structure – XANES

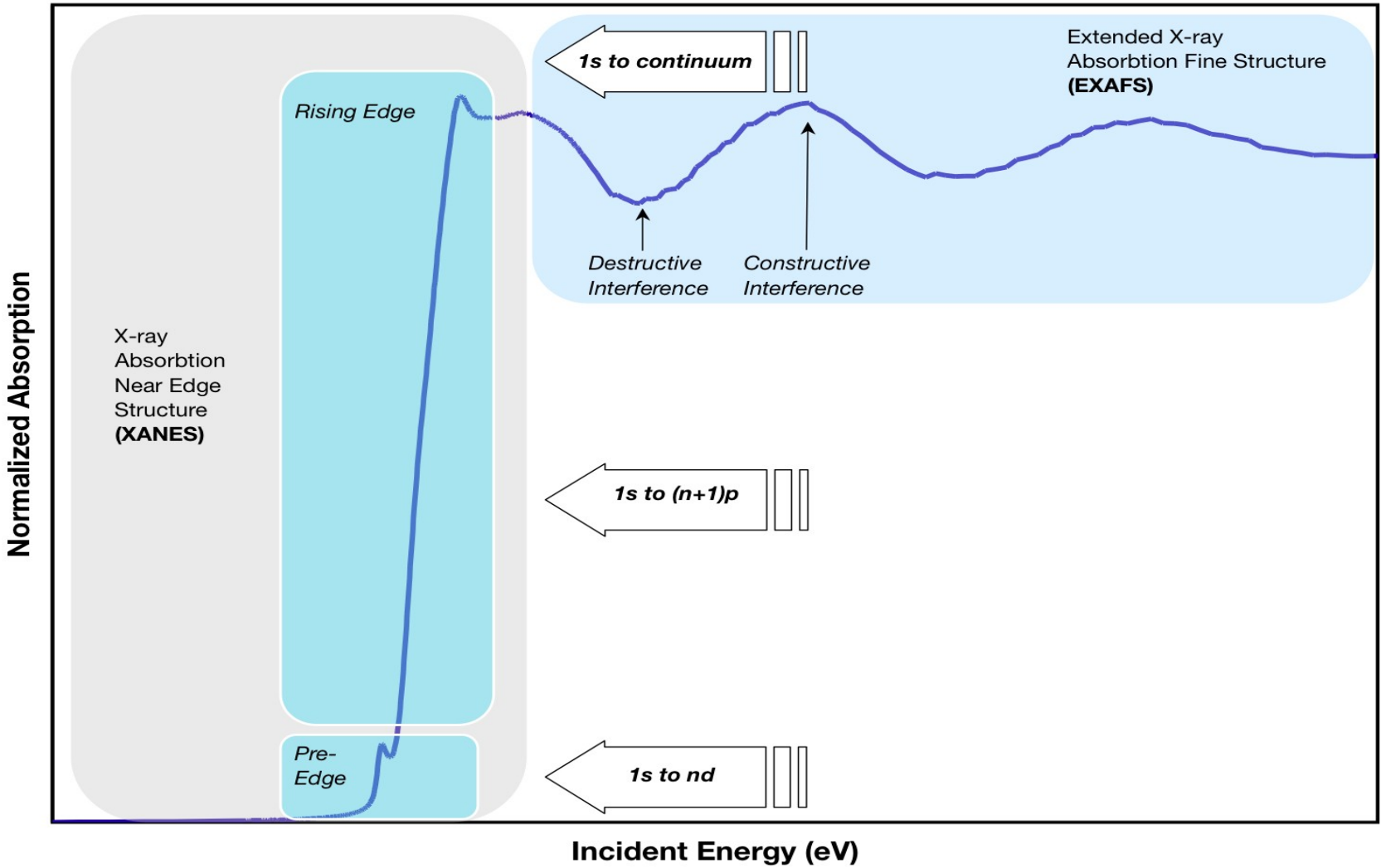

XAFS

Rentgenová absorpční spektroskopie jemné struktury
Uspořádání experimentu ESRF BM26A

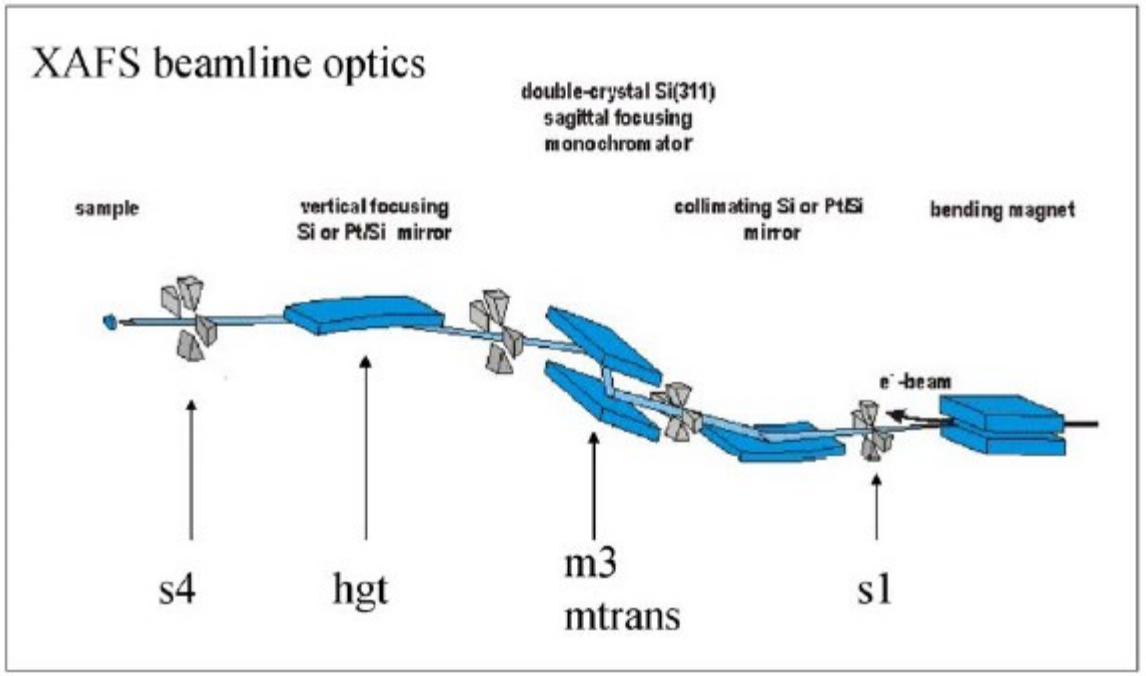

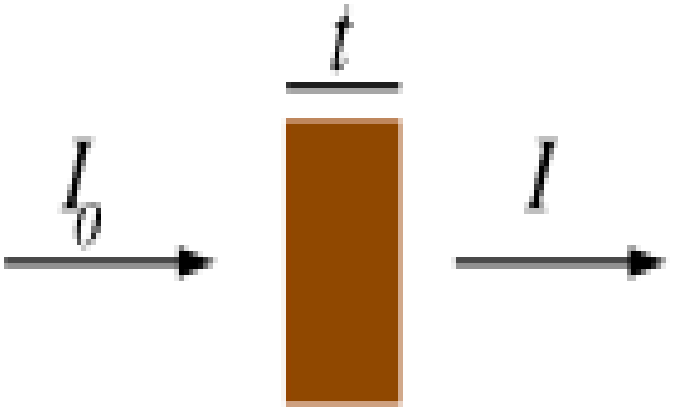

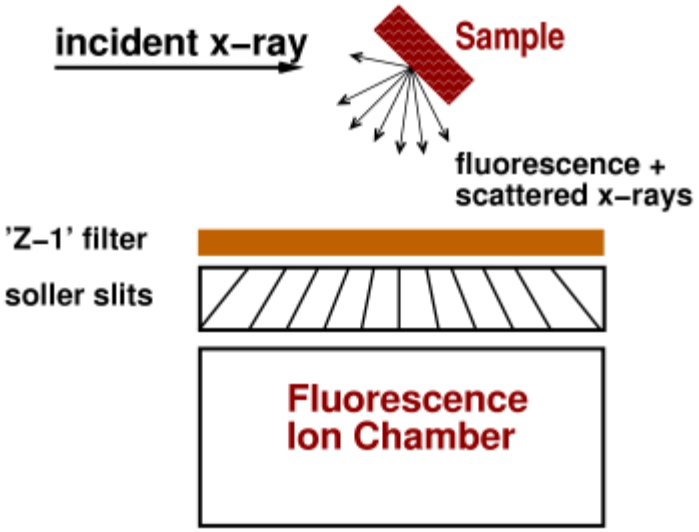

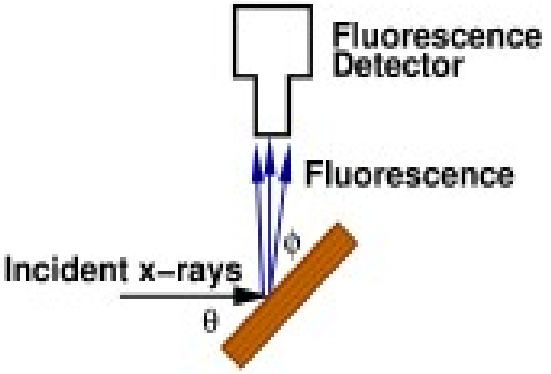

XAFS

Rentgenová absorpční spektroskopie jemné struktury
Uspořádání experimentu

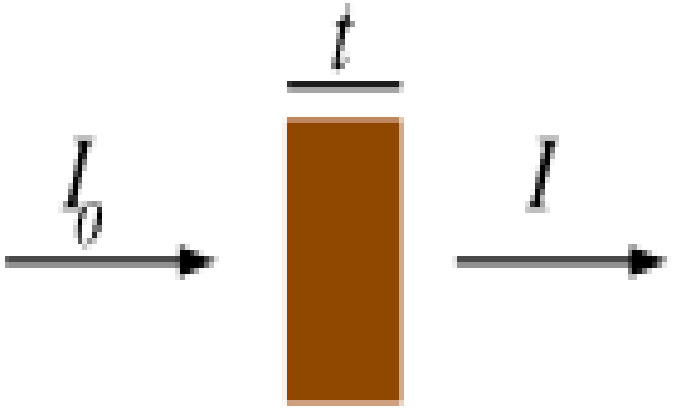

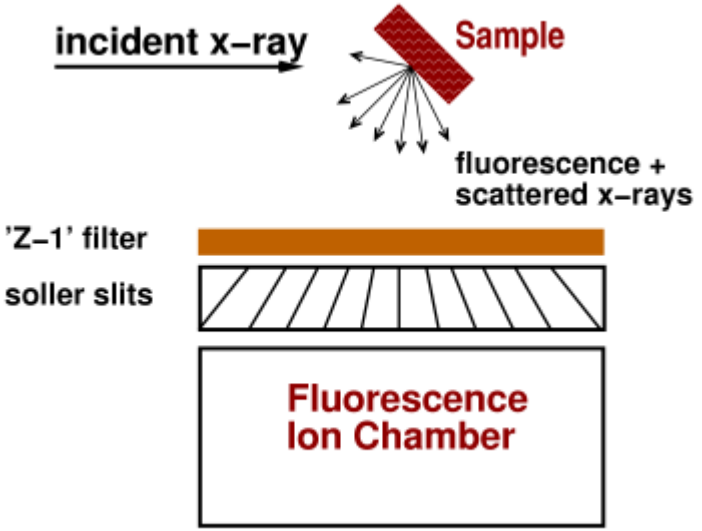

Electron yield measurement

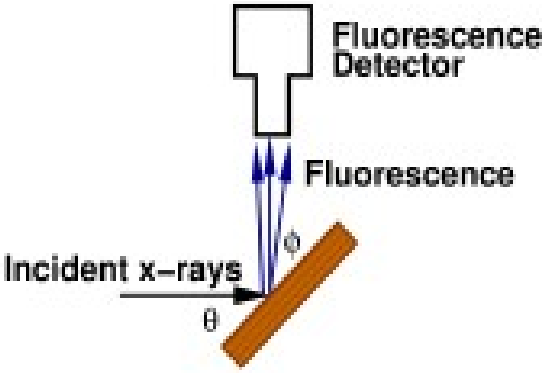

XAFS

Rentgenová absorpční spektroskopie jemné struktury

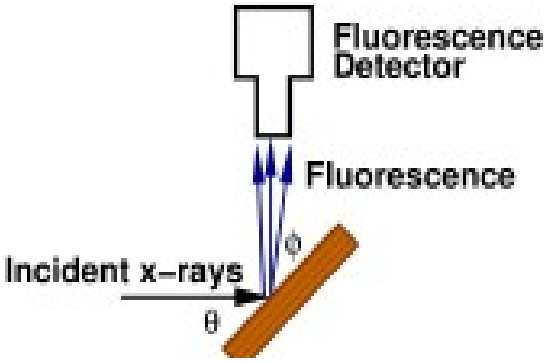

$$\mu(E) \propto I_f / I_0.$$

$$I_f = I_0 \frac{\epsilon \Delta\Omega}{4\pi} \frac{\mu_\chi(E)\left\{1 - e^{-[\mu_{\mathrm{tot}}(E)/\sin\theta + \mu_{\mathrm{tot}}(E_f)/\sin\phi]t}\right\}}{\mu_{\mathrm{tot}}(E)/\sin\theta + \mu_{\mathrm{tot}}(E_f)/\sin\phi}$$

$$\mu_{\mathrm{tot}}(E) = \mu_\chi(E) + \mu_{\mathrm{other}}(E)$$

XAFS

Rentgenová absorpční spektroskopie jemné struktury

Eq. 4.2 has several interesting limits that are common for real XAFS measurements. First, there is the *thin sample limit*, for which $\mu t \ll 1$. The $1 - e^{-\mu t}$ term then becomes $\approx [\mu_{\rm tot}(E)/\sin\theta + \mu_{\rm tot}(E_f)/\sin\phi]\, t$ (by a Taylor series expansion), which cancels the denominator, so that

$$I_f \approx I_0 \frac{\epsilon \Delta\Omega}{4\pi} \mu_\chi(E) t \tag{4.4}$$

Alternatively, there is the *thick, dilute sample limit*, for which $\mu t \gg 1$ and $\mu_\chi \ll \mu_{\rm other}$. Now the exponential term goes to 0, so that

$$I_f = I_0 \frac{\epsilon \Delta\Omega}{4\pi} \frac{\mu_\chi(E)}{\mu_{\rm tot}(E)/\sin\theta + \mu_{\rm tot}(E_f)/\sin\phi}. \tag{4.5}$$

Finally, One way to reduce these self-absorption effects for thick, concentrated samples is to rotate the sample so that the sample is normal to the incident beam. With $\phi \to 0$ or the *grazing exit limit*, $\mu_{\rm tot}(E_f)/\sin\phi \gg \mu_{\rm tot}(E)/\sin\theta$, giving

$$I_f \approx I_0 \frac{\epsilon \Delta\Omega}{4\pi} \frac{\mu_\chi(E)}{\mu_{\rm tot}(E_f)/\sin\phi} \tag{4.7}$$

XANES

Profil absorpční hrany závisí na chemickém stavu atomu. Nutný kvantově-mechanický výpočet.
Přechod z hluboké hladiny do volných stavů nad Fermiho mezí.

Příklad pro železo v různých chemických stavech.

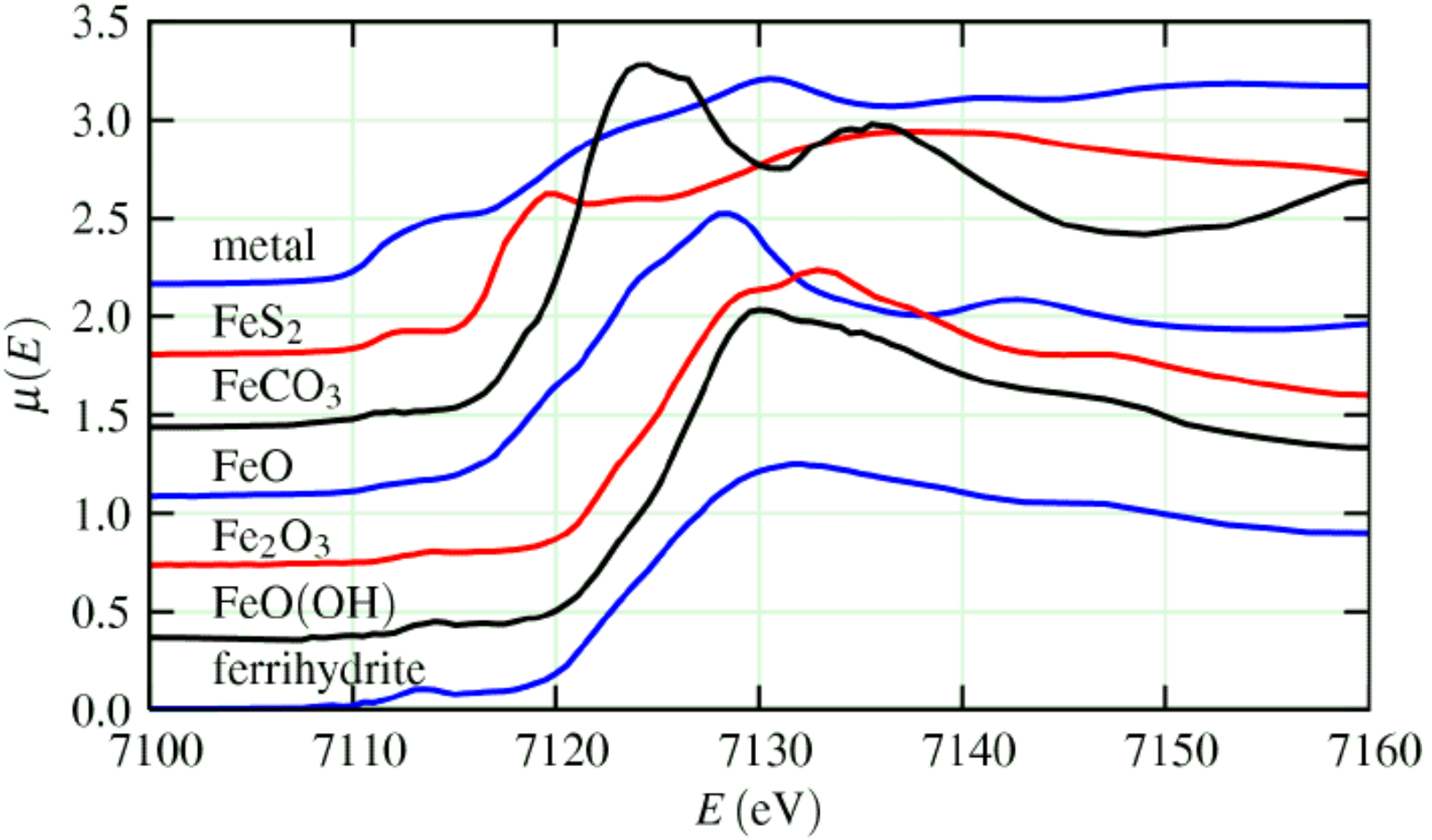

EXAFS

Jemná struktura okolí absorpční hrany – určení poloh nejbližších atomů.

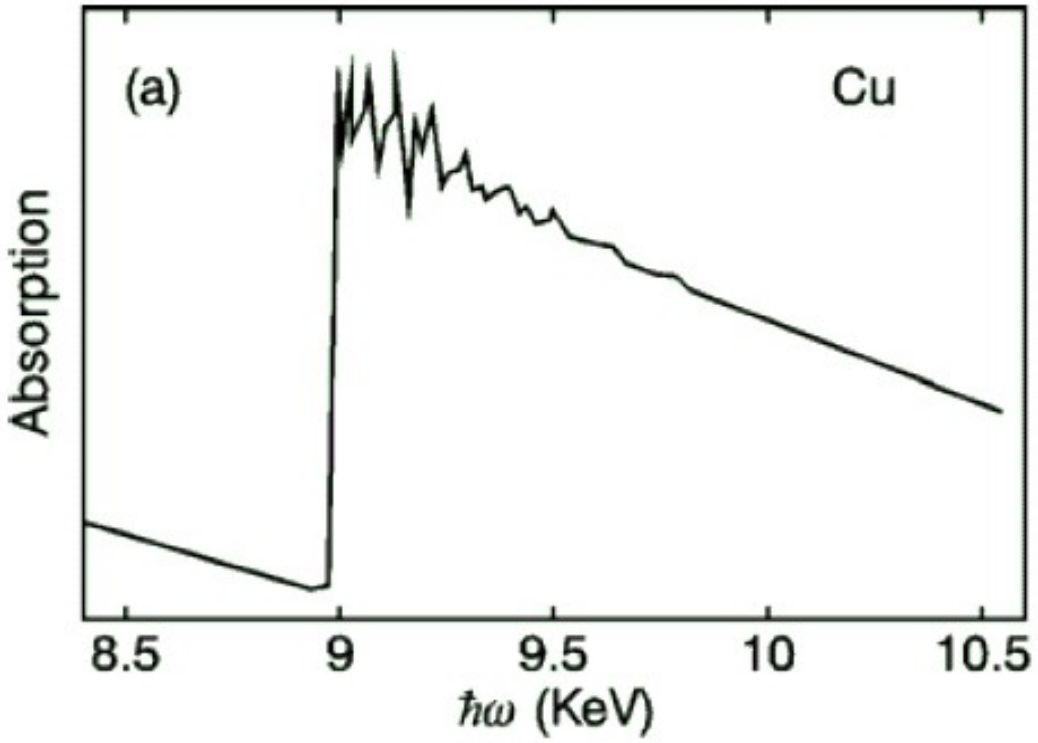

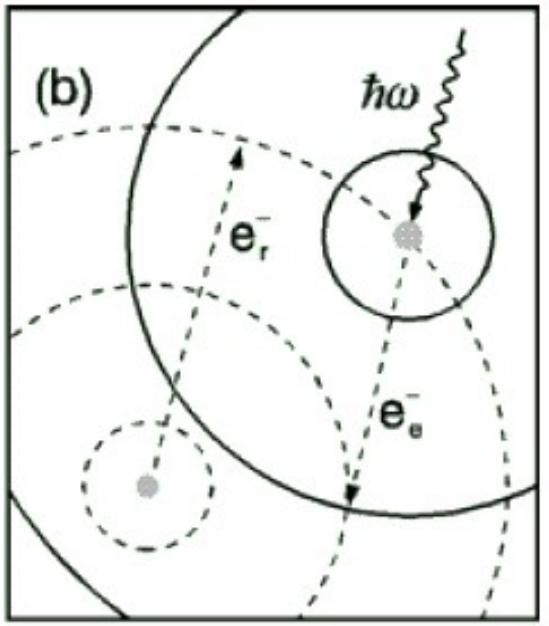

Propustnost $$T(\epsilon) = \mathrm{e}^{-\mu(\epsilon)t}$$

Normovaná absorpce $$\chi(\epsilon) = \frac{\mu(\epsilon) - \mu_0}{\Delta\mu_{\mathrm{edge}}}$$

EXAFS

Vlnový vektor
excitovaného elektronu

$$k_{\mathrm{e}}^2 = \frac{2m_{\mathrm{e}}}{\hbar^2}(\epsilon - \epsilon_0)$$

Příspěvek jednoho atomu ve vzdálenosti *R*

$$\chi(k) = \frac{f(k)}{kR^2}\,\sin[2kR + \delta(k)]$$

Celková amplitude středovaná přes polohy a typ sousedů

Závislost úměrná R^{-2} – citlivé maximálně na třetí nejbližší sousedy.

EXAFS

Příspěvek jednoho atomu ve vzdálenosti *R*

$$\chi(k) = \sum_j \frac{N_j e^{-2k^2\sigma_j^2} e^{-2R_j/\lambda(k)} f_j(k)}{kR_j^2} \sin[2kR_j + \delta_j(k)]$$

Celková amplitude středovaná přes polohy a typ sousedů

Závislost úměrná R^{-2} – citlivé maximálně na třetí nejbližší sousedy.

EXAFS

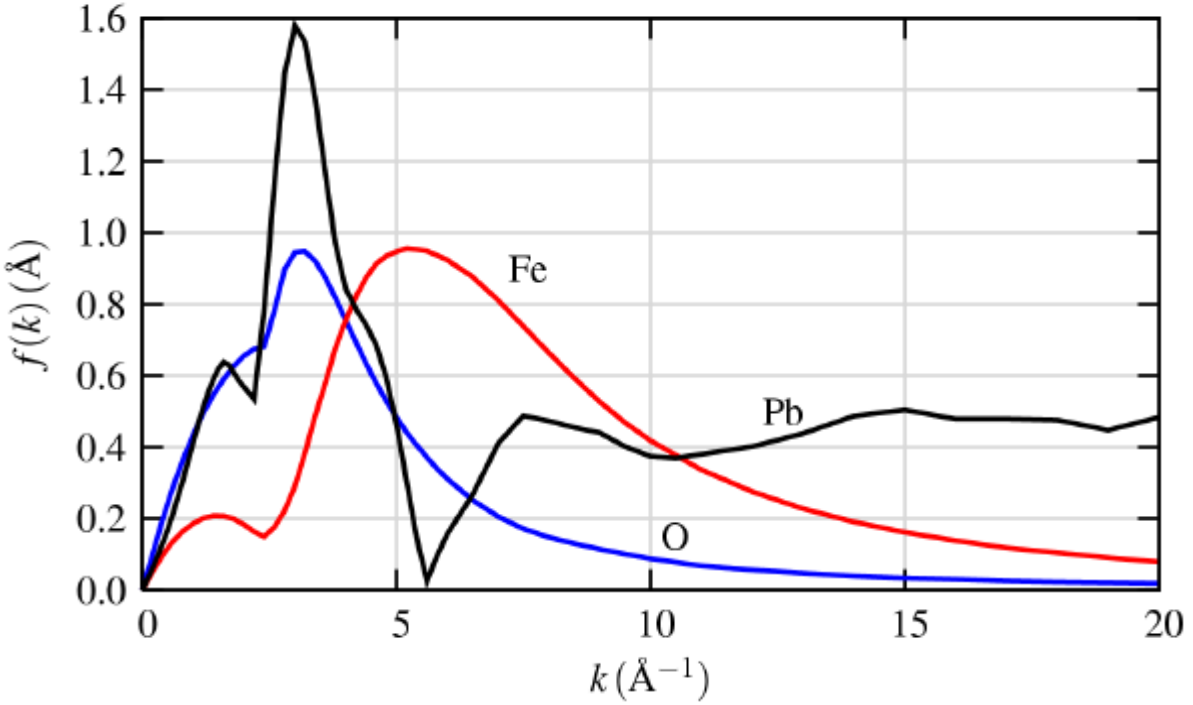
1.6
1.4
1.2
1.0
0.8
0.6
0.4
0.2
0.0
$f(k)$ (Å)
Fe
Pb
O
0
5
10
15
20
k (Å^{-1})

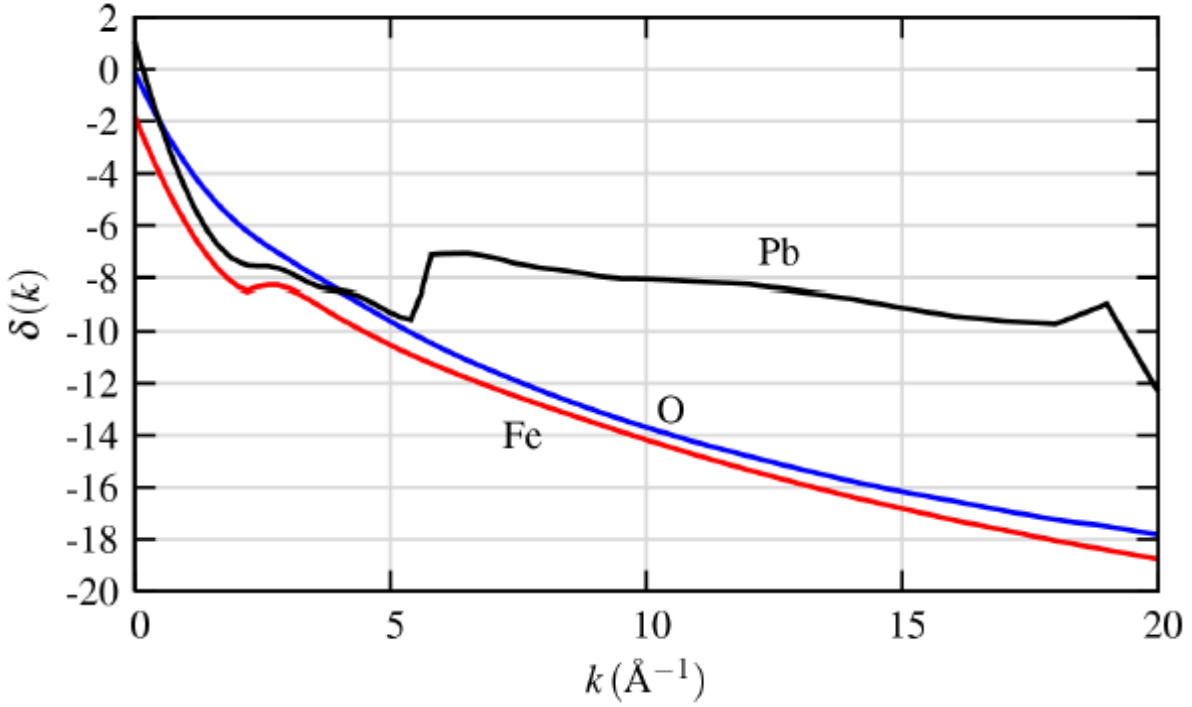
2
0
-2
-4
-6
-8
-10
-12
-14
-16
-18
-20
$\delta(k)$
Pb
O
Fe
0
5
10
15
20
k (Å^{-1})

EXAFS

Normovaný koeficient absorpce pro měď.
Měření čárkovaně, simulace plnou čarou.

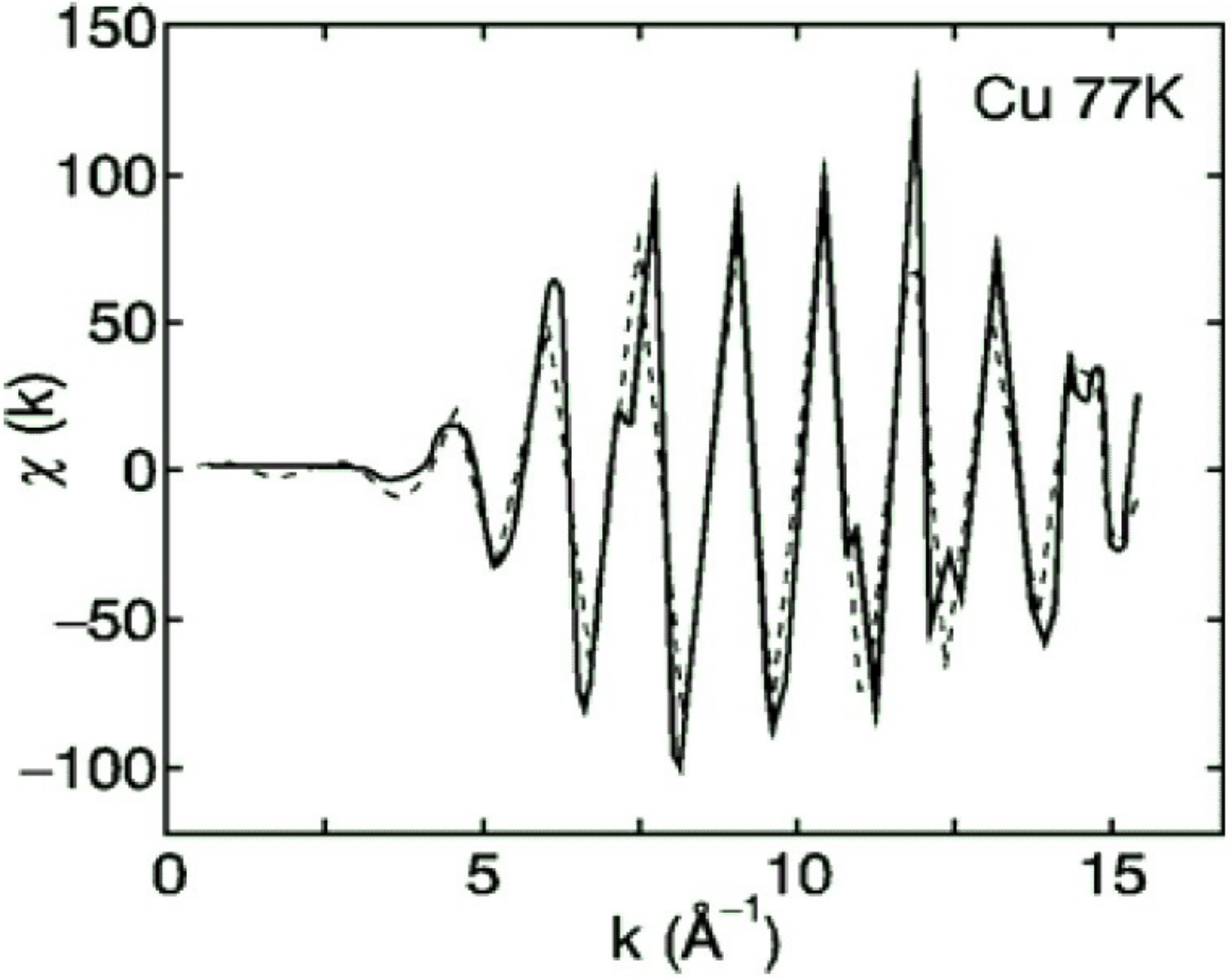

EXAFS

Fe-O data

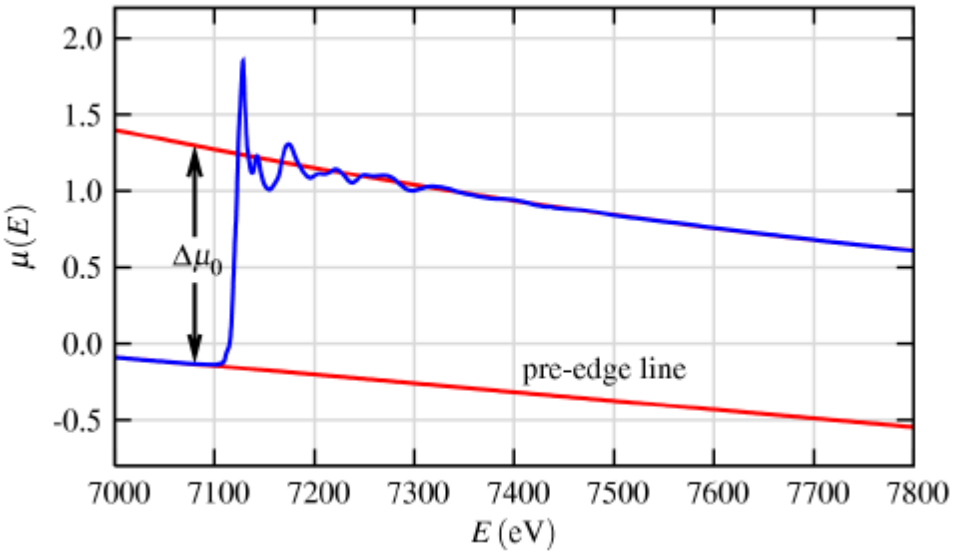

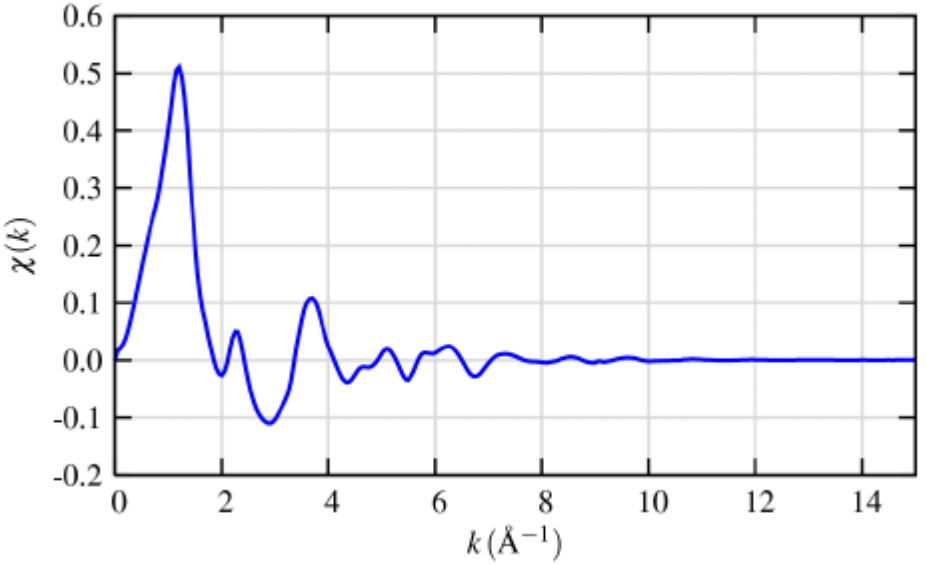

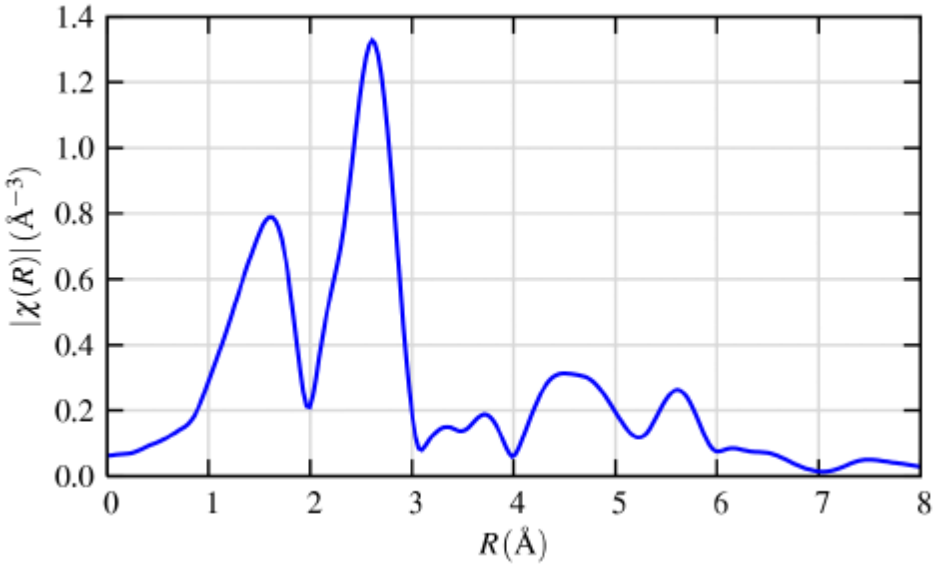

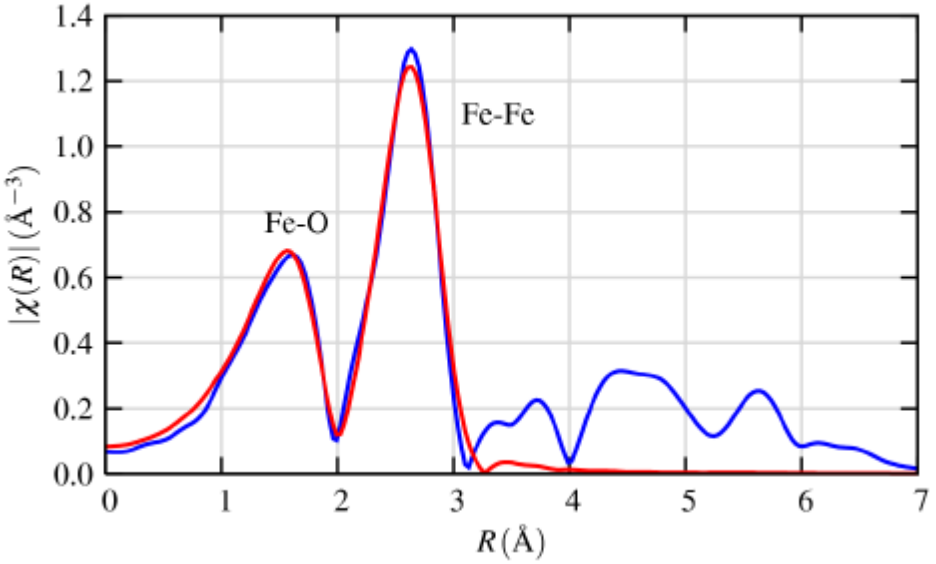

EXAFS + XANES analytický software

- FEFF
- FDMNES
- Demeter (Bruce Ravel):
  - Athena
  - Artemis
  - Hephaestus

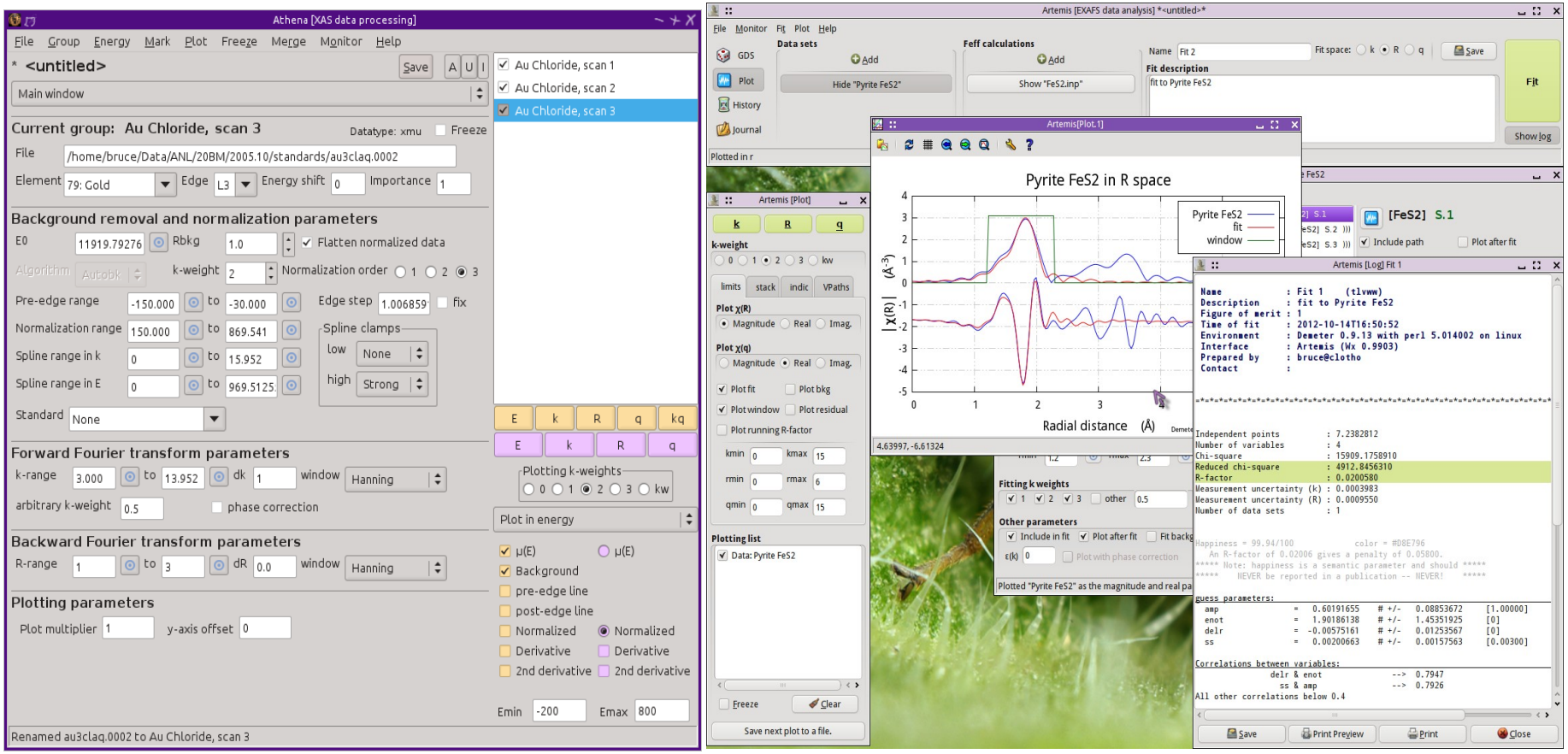

EXAFS

Mn in BiTe

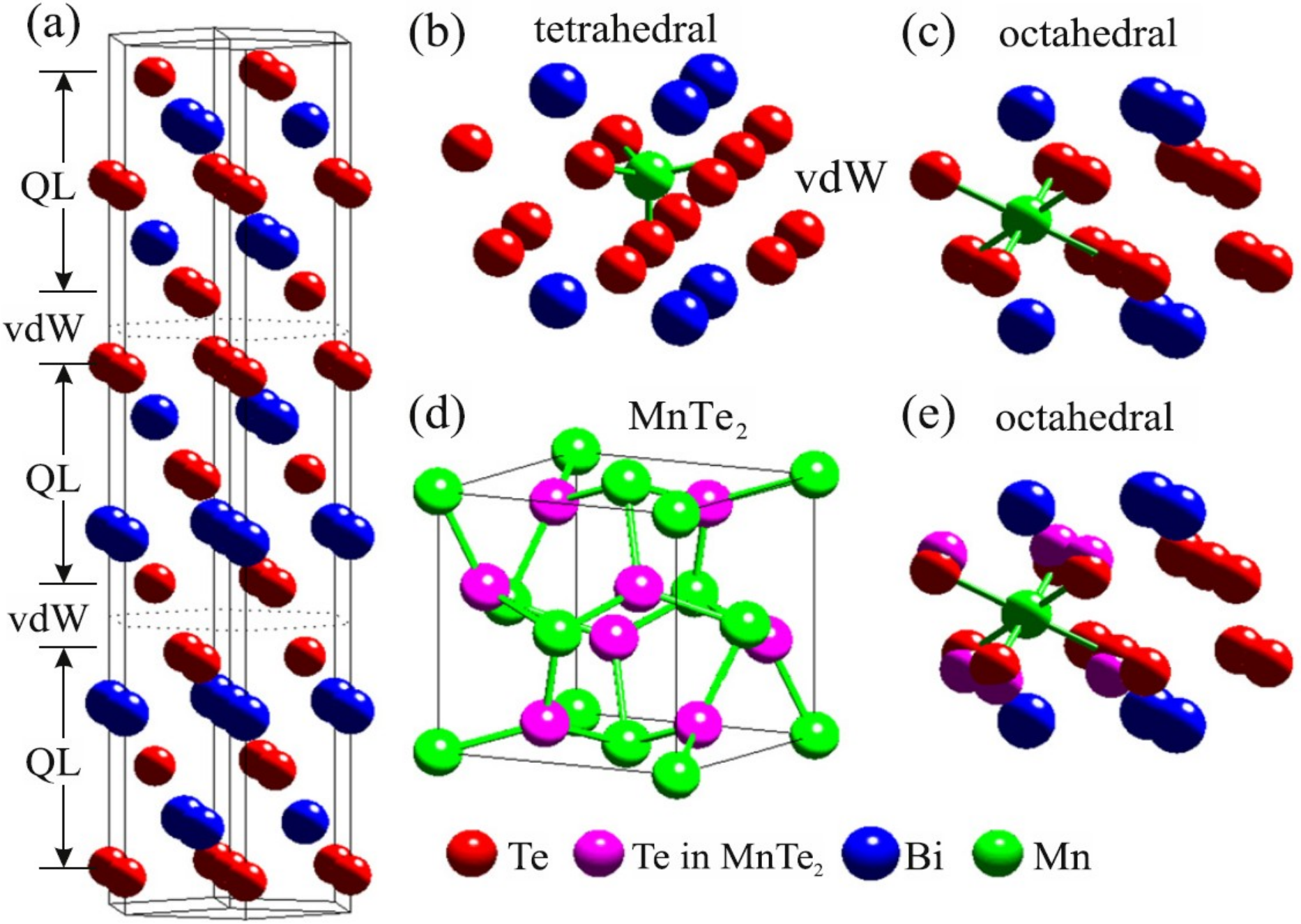

EXAFS

Mn in BiTe

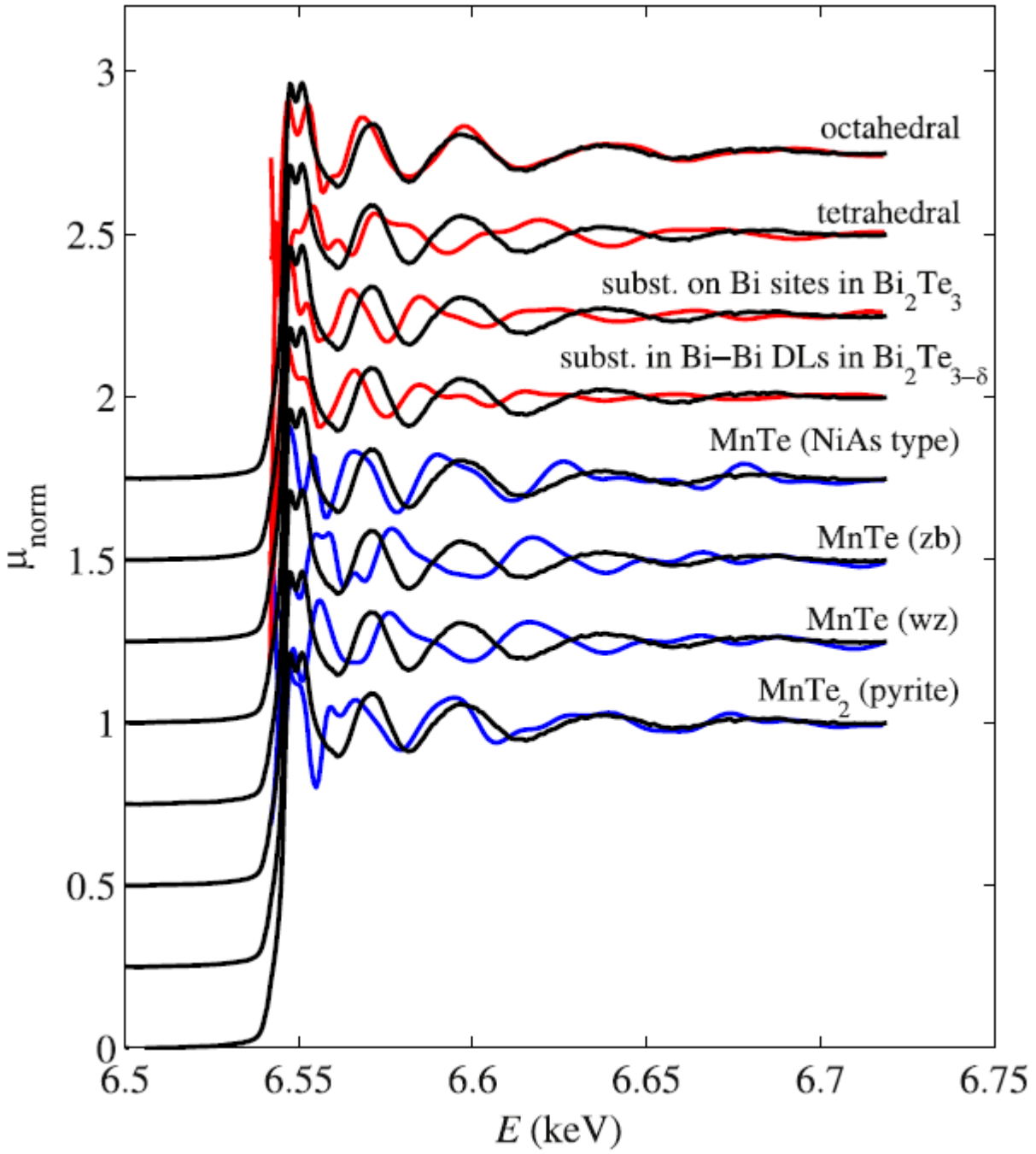

EXAFS

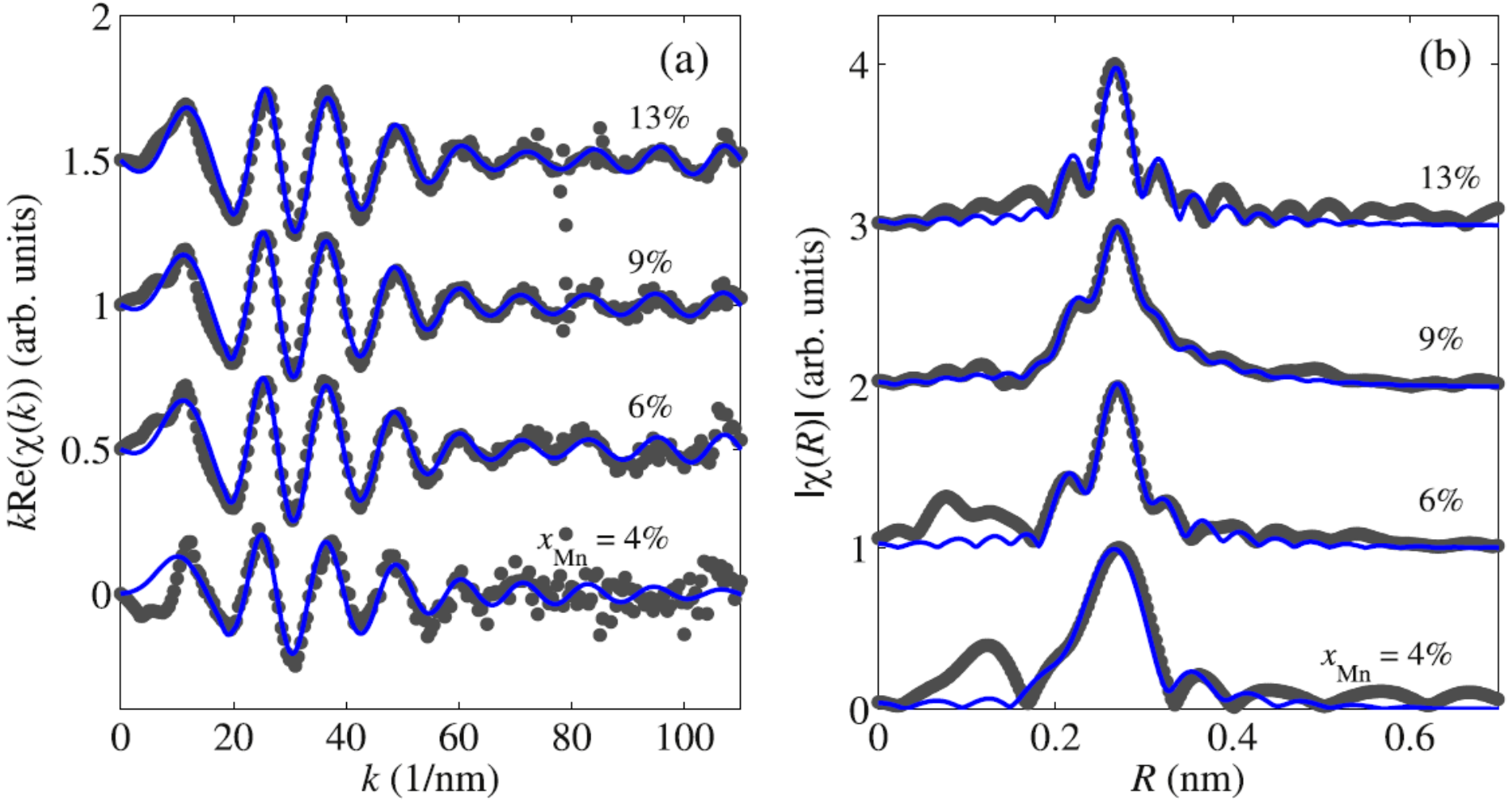

x_{Mn} (%)	d_{Mn-Te} (nm)	d_{Mn-Bi} (nm)
4	0.290 ± 0.009	—
6	0.292 ± 0.004	0.304 ± 0.010
9	0.292 ± 0.004	0.303 ± 0.010
13	0.291 ± 0.006	0.306 ± 0.014

XMCD

Absorpce na hladinách s orbitálním momentem

Povrchově citlivé,
Prvkově citlivé

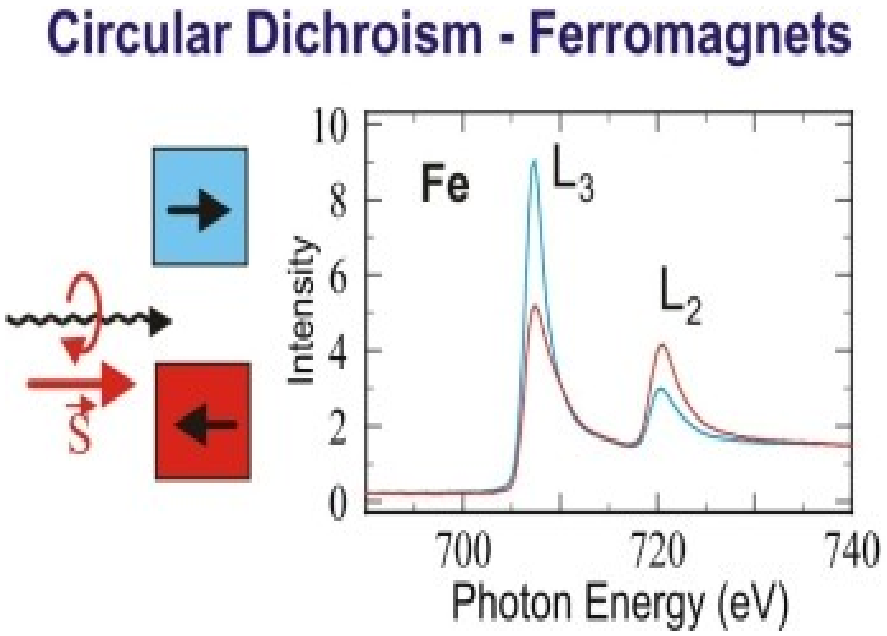

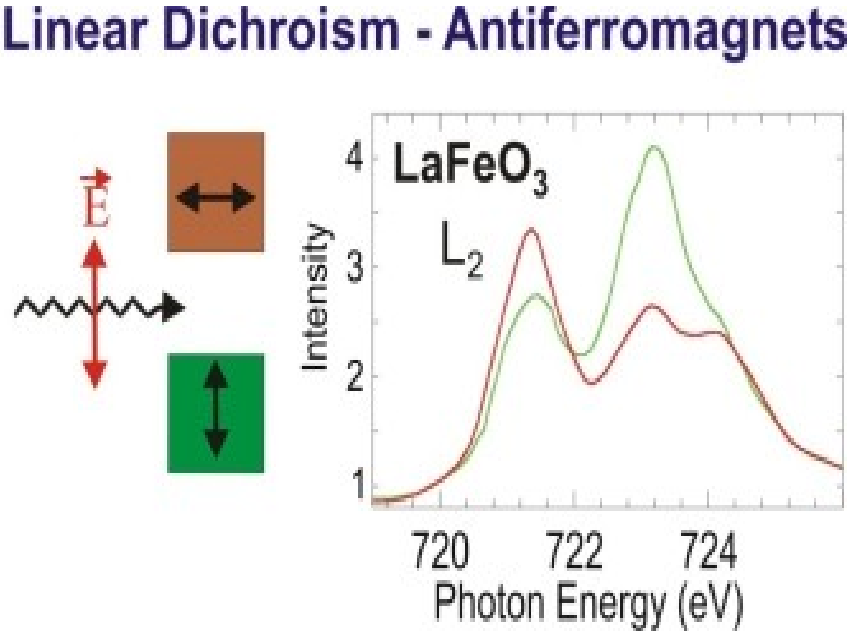

Asymmetry $A=(I_+-I_-)/(I_++I_-)$

XMCD

Absorpce na hladinách s nenulovým orbitálním momentem (vyšší než K)

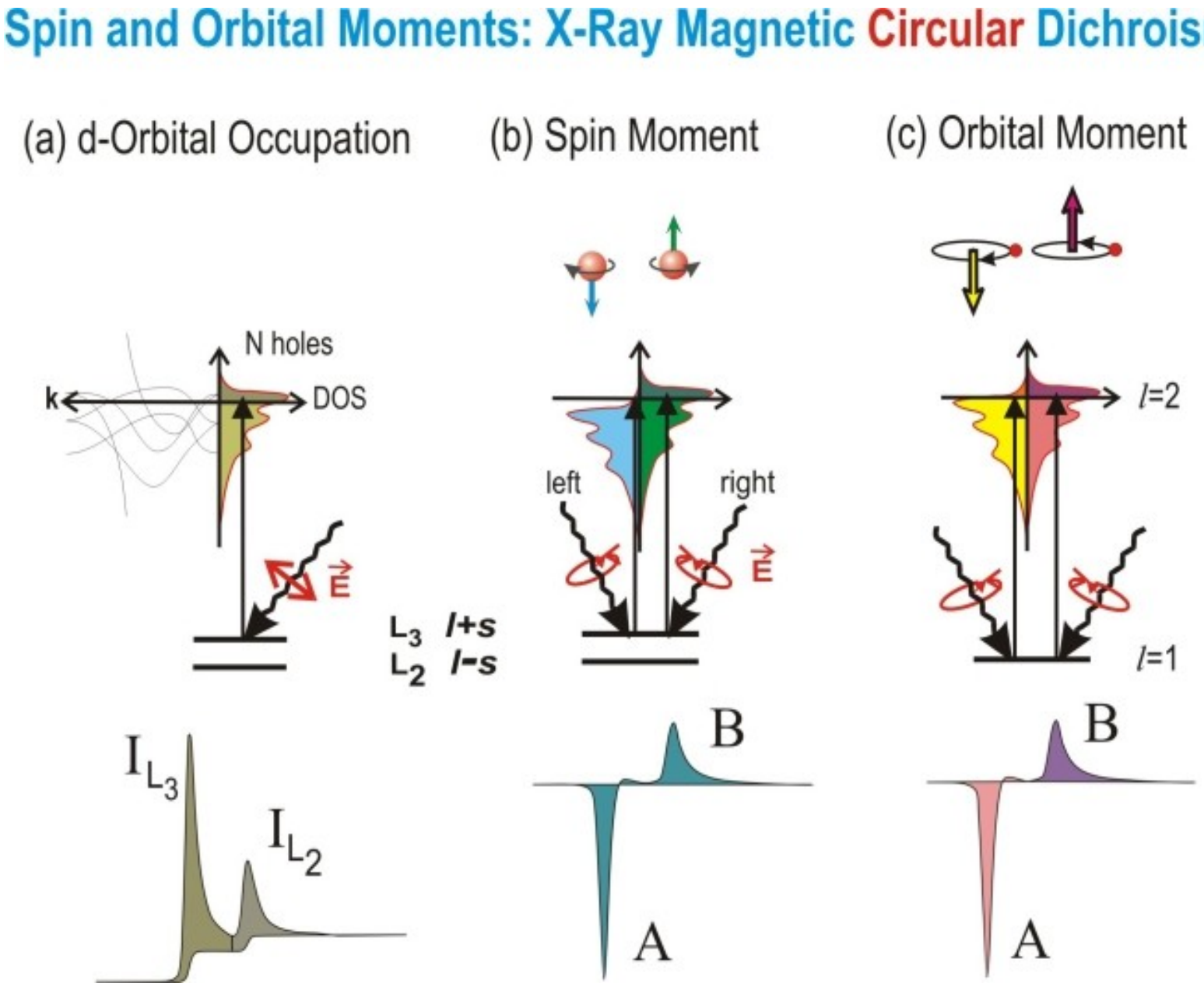

X-rays absorption and X-ray magnetic circular dichroism (XMCD)

Two step model:

1) spin-polarized photoelectrons are created by using circularly polarized x-rays
2) these polarized photoelectrons are used to analyze the spin-split valence density of states, thus the valence band acts as a spin-sensitive detector.

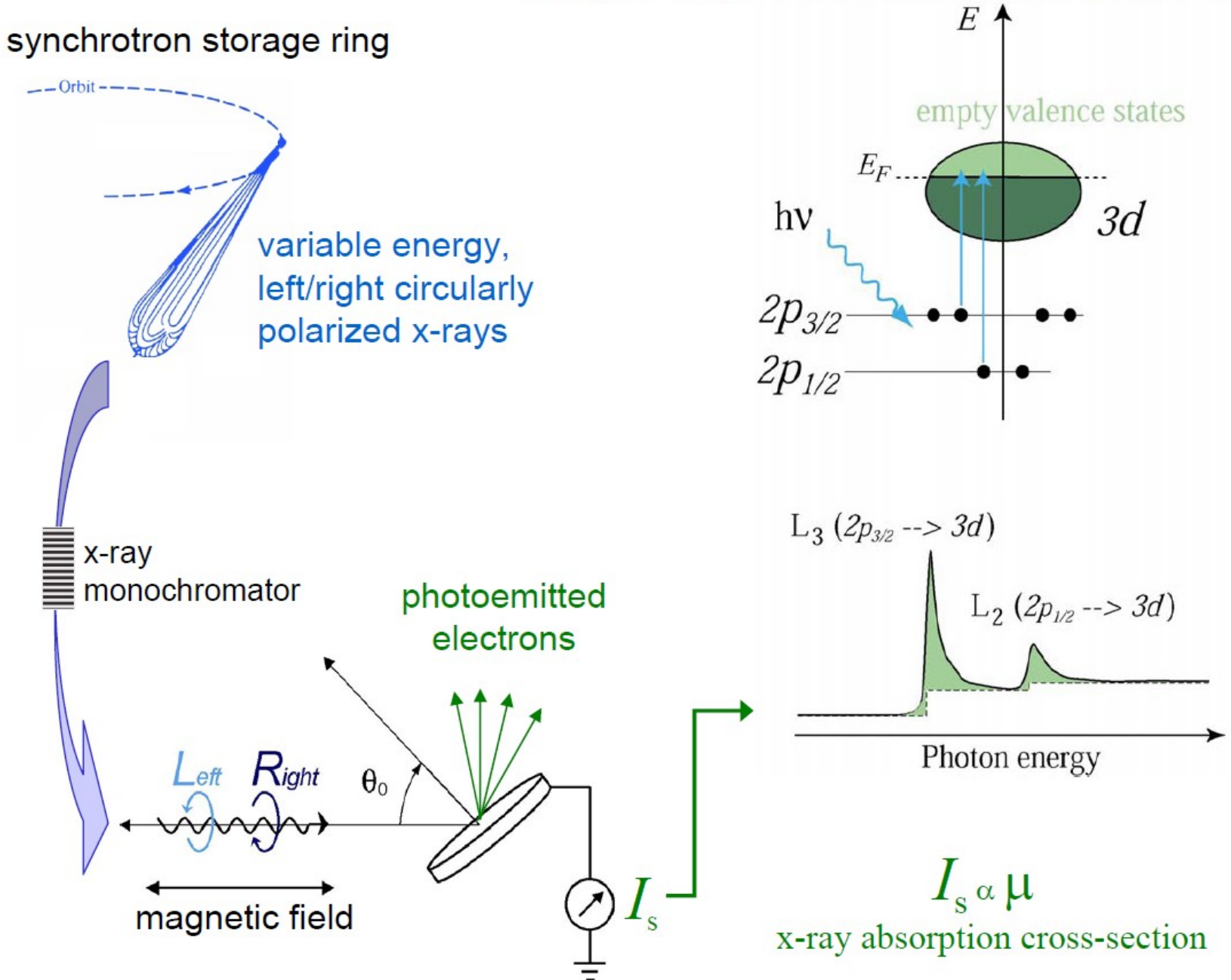

XMCD theory: basic idea

Photon-electron interaction: dipole approximation $H_{int}(0,t) \approx \underline{r}\cdot\underline{\varepsilon}_q \, [a_k \exp(-i\omega_k t) + c.c.]$

The dipole operator $P_q^{1} = \underline{r}\cdot\underline{\varepsilon}_q$ can be written in terms of Racah's tensor operators (where $Y_{l,m}$ are the spherical harmonics)

$\underline{\varepsilon}_q$ is the polarization dependent electric vector

q = 0 -> linear polarization
q = +/- 1 -> circular polarization

$$P_{\pm1}^{(1)} = \mp\frac{1}{\sqrt{2}}(x \pm iy) = rC_{\pm1}^{(1)} = r\sqrt{\frac{4\pi}{3}}Y_{1,\pm1}$$

$$P_0^{(1)} = z = rC_0^{(1)} = r\sqrt{\frac{4\pi}{3}}Y_{1,0}$$

The photon absorption generates a transition from an initial core level to a final level close to the Fermi level (note that the spin is not affected)

$$|i\rangle = R_i(r)\,|c, m_c; s = \frac{1}{2}, m_s\rangle \longrightarrow |f\rangle = R_f(r)\,|l, m_l; s = \frac{1}{2}, m_s\rangle$$

$\langle l,m\|C_{\pm1}^{(1)}\|l-1,m\mp1\rangle = \sqrt{\frac{(l\pm m)(l\pm m-1)}{2(2l-1)(2l+1)}}$	$\langle l,m\|C_{\pm1}^{(1)}\|l+1,m\mp1\rangle = -\sqrt{\frac{(l\mp m+2)(l\mp m+1)}{2(2l+3)(2l+1)}}$
$= \sqrt{\frac{l(l-1)\pm(2l-1)m+m^2}{2(2l-1)(2l+1)}}$	$= -\sqrt{\frac{l(l+3)\mp(2l+1)m+m^2}{2(2l+3)(2l+1)}}$
$\langle l,m\|C_0^{(1)}\|l-1,m\rangle = \sqrt{\frac{l^2-m^2}{(2l-1)(2l+1)}}$	$\langle l,m\|C_0^{(1)}\|l+1,m\rangle = \sqrt{\frac{(l+1)^2-m^2}{(2l+3)(2l+1)}}$

Table 1.3: Electric dipole matrix elements $\langle l, m_l|C_q^{(1)}|c, m_c\rangle$ in the one electron model. The matrix elements are non-vanishing when $c = l-1$ (left column) or $c = l+1$ (right column), and when $m_c + q = m_l$. q denotes the state of polarization of the photons which mix the states $|l, m_l\rangle$ and $|c, m_c\rangle$.

Remember: things become easily complicate. For example, if spin-orbit interaction is not negligible the (L, m_L, S, m_S) is not the good basis and you have to use the (L, S, J, m_J) basis

X-rays absorption and X-ray magnetic circular dichroism (XMCD)

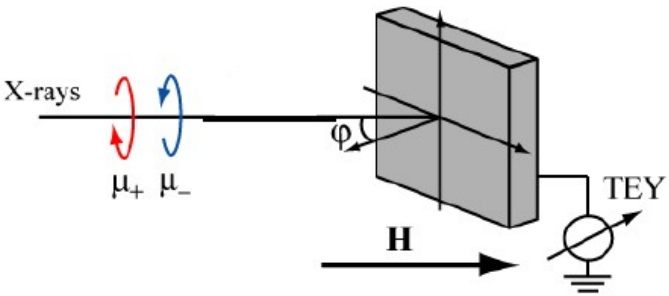

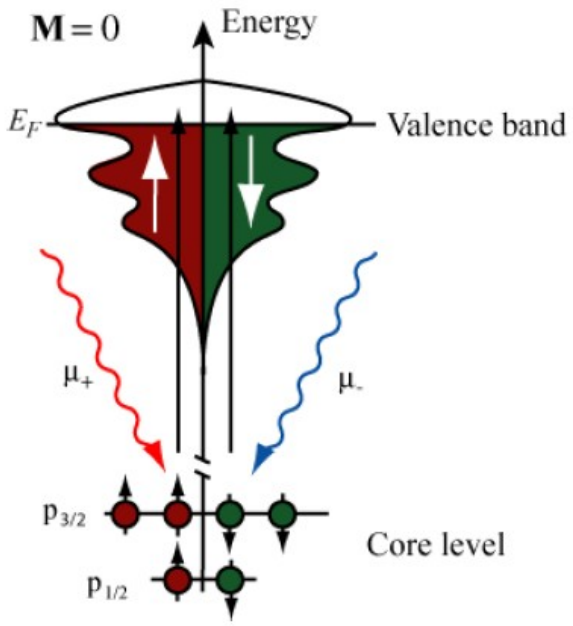

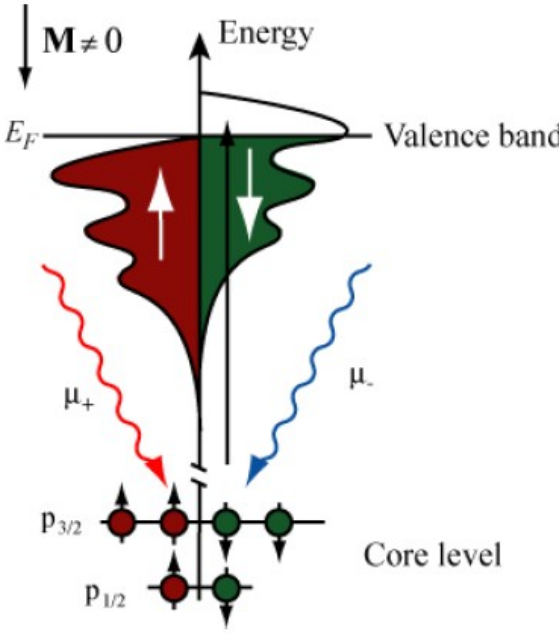

μ in dipole approximation

$$\mu \propto \left|\left\langle f \left| \varepsilon r \right| i \right\rangle\right|^2 \delta(\hbar\omega - (E_f - E_i))\rho(E_f)$$

Dipole selection rules

$\Delta l = \pm 1, \Delta s = 0$ 2p → 3d, 4s

$\Delta m_l = +1$ right circular

$\Delta m_l = -1$ left circular

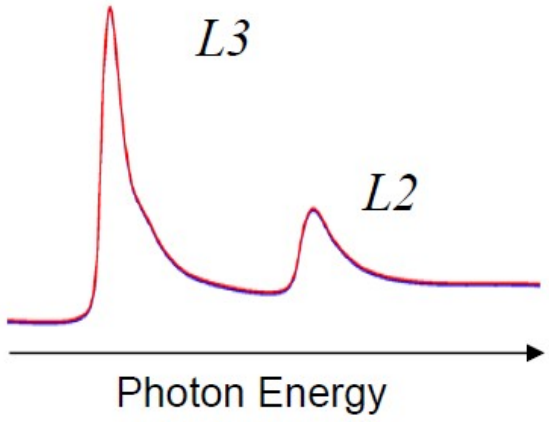

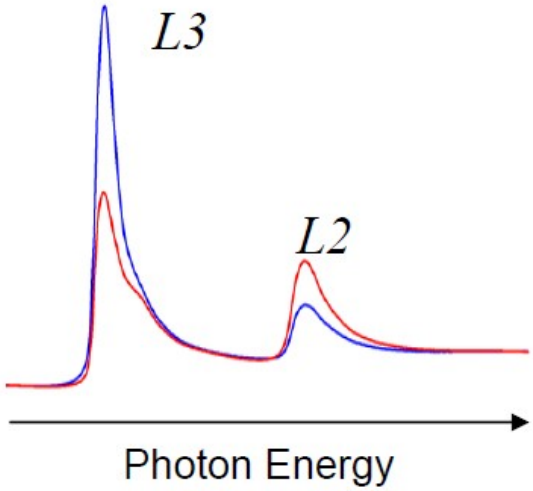

X-rays absorption and X-ray magnetic circular dichroism (XMCD)

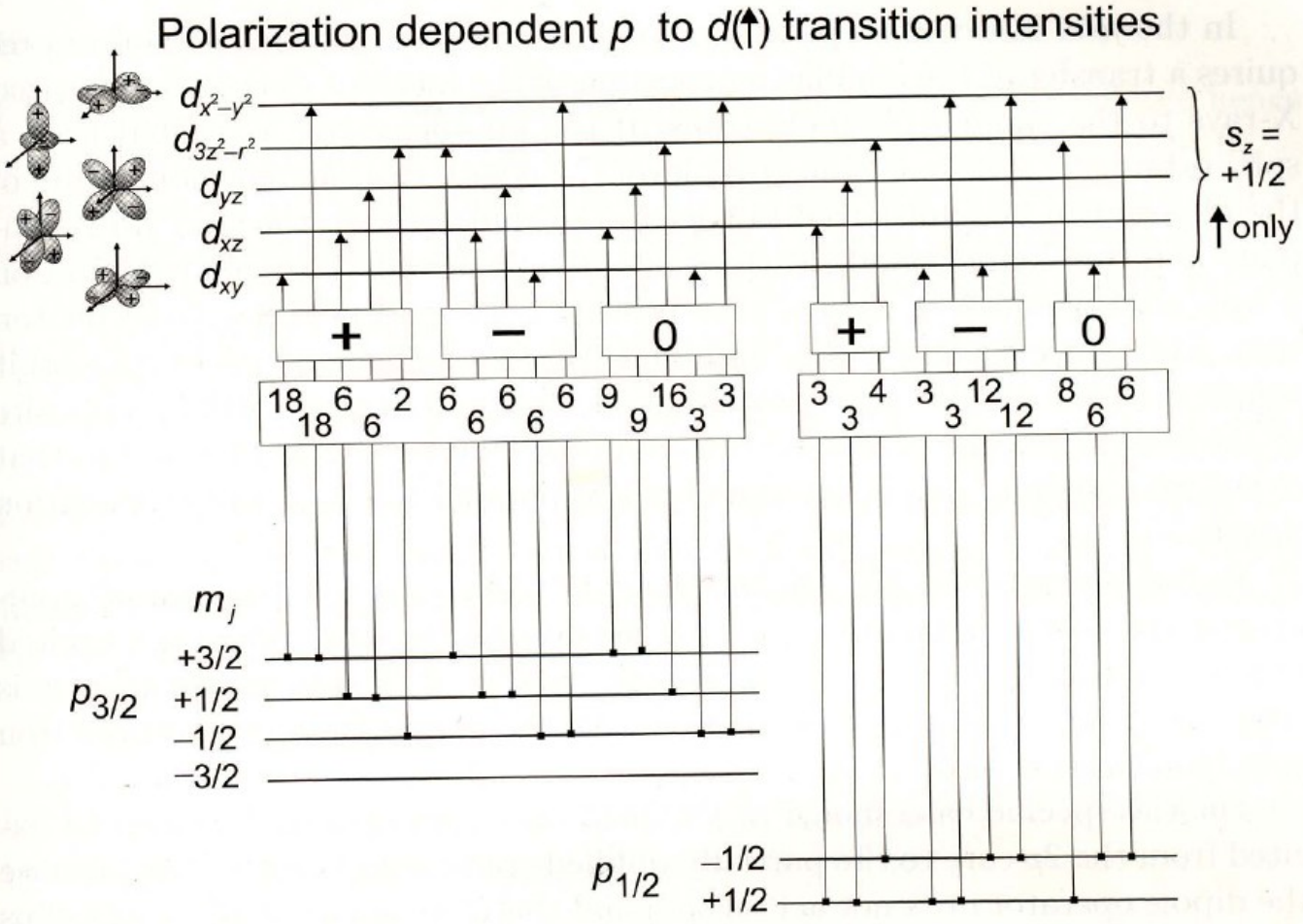

Fig. 9.14. Polarization dependent transition intensities in a one-electron model from spin–orbit and exchange split p core states $|j, m_j\rangle$ to *spin-up* ($m_s = +1/2$) d valence orbitals (Table A.2), assumed to be split by the exchange interaction. The listed intensities each need to be divided by 90 to get the proper absolute values in units of $\mathcal{AR}^2$. We have chosen the z-axis as the spin quantization axis and the transition intensities are for circular polarization with $\boldsymbol{k} \parallel z$ and angular momenta $q = +1$ (labeled +) and $q = -1$ (labeled −) and for linear polarization with $\boldsymbol{E} \parallel z$ (labeled $q = 0$). We have assumed a splitting of the p states by the exchange interaction, lifting the degeneracy in m_j. Note that this causes an opposite order of m_j states for $p_{3/2}$, $l + s$ and $p_{1/2}$, $l - s$ because of the opposite sign of s

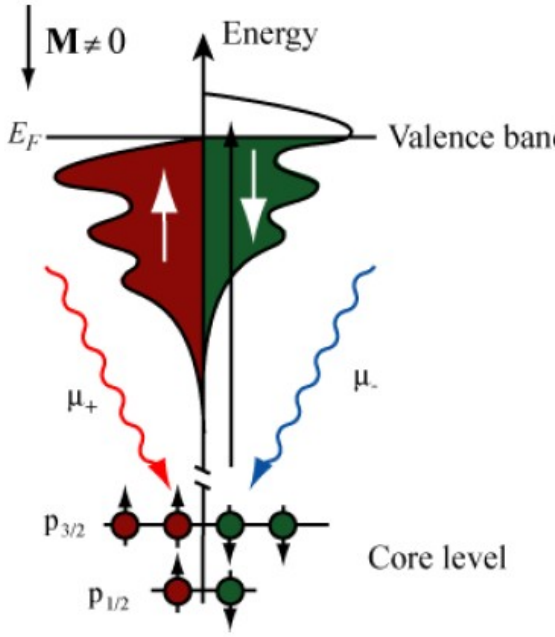

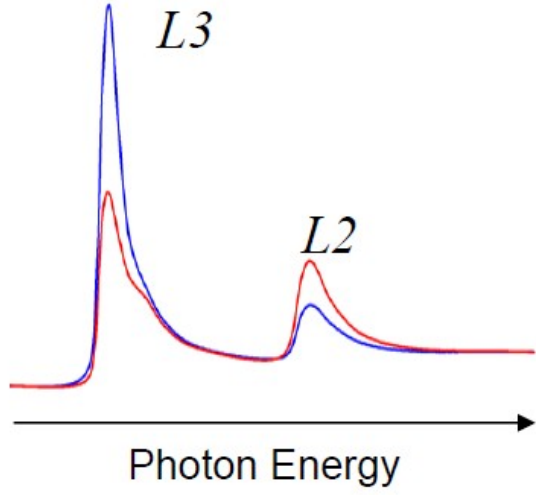

XMCD

Generace polarizovaného rtg záření

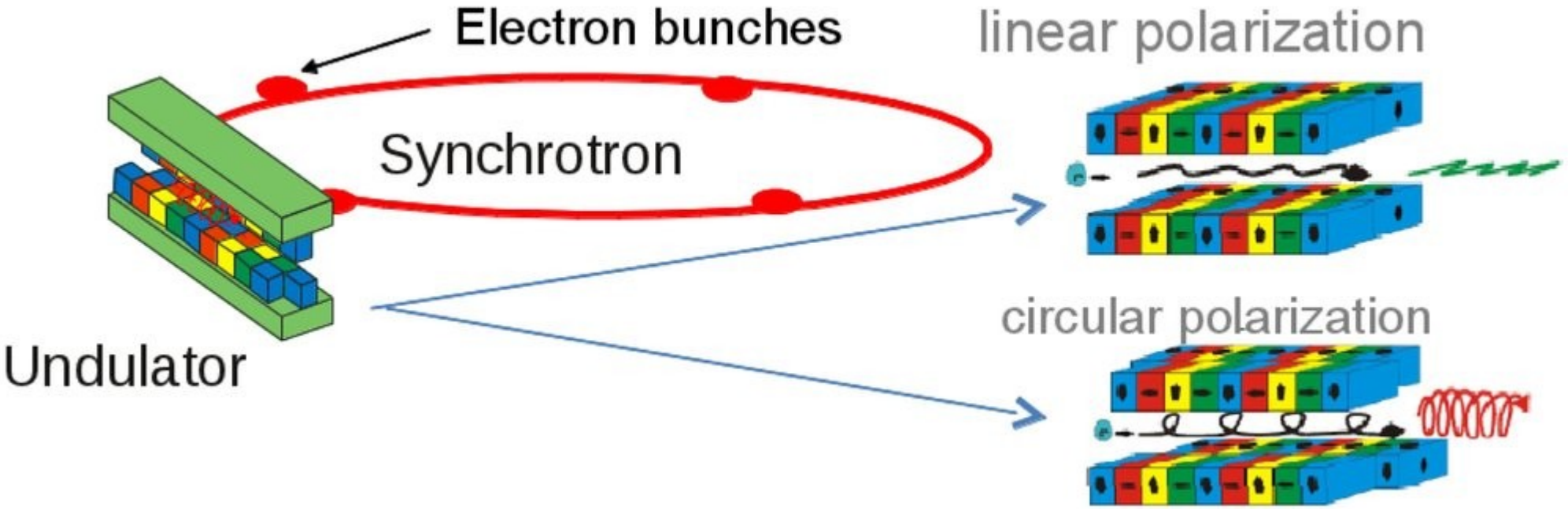

XMCD

Generace polarizovaného rtg záření

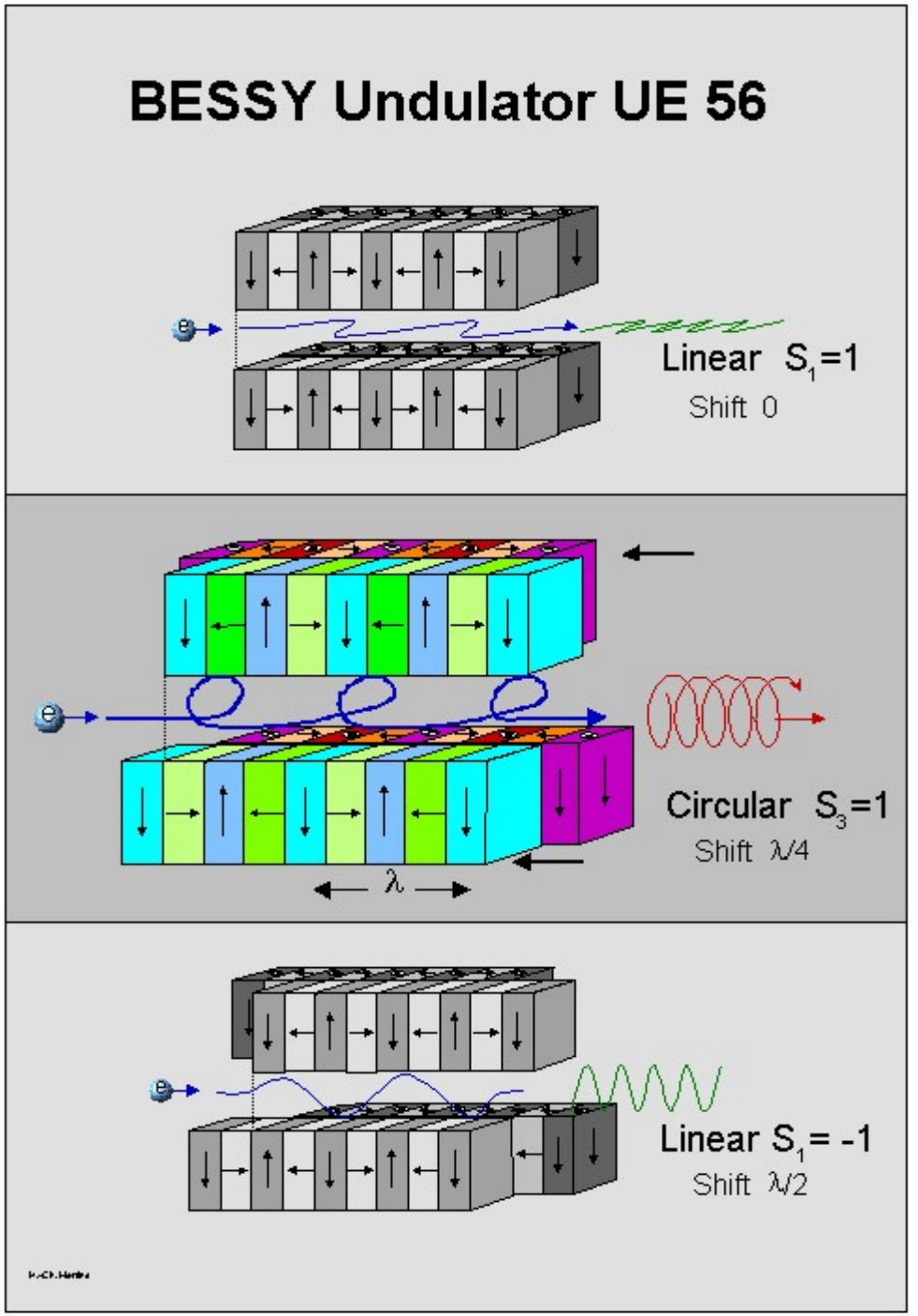

XMCD

Lineární polarizátor pro
rtg záření

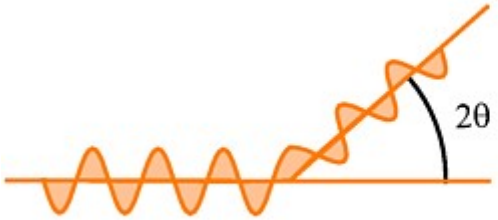

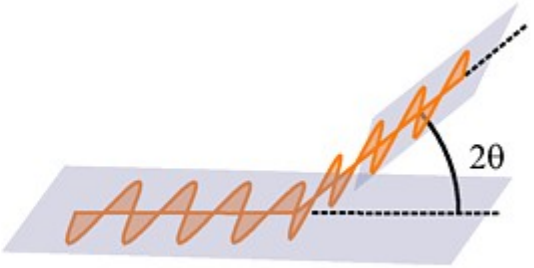

Case (1): P-Polarisation in plane of scattering, $P = \cos^2 2\theta$
Case (2): S-Polarisation perpendicular to plane of scattering, $P = 1$

“Brewsterův úhel” = 45 stupňů

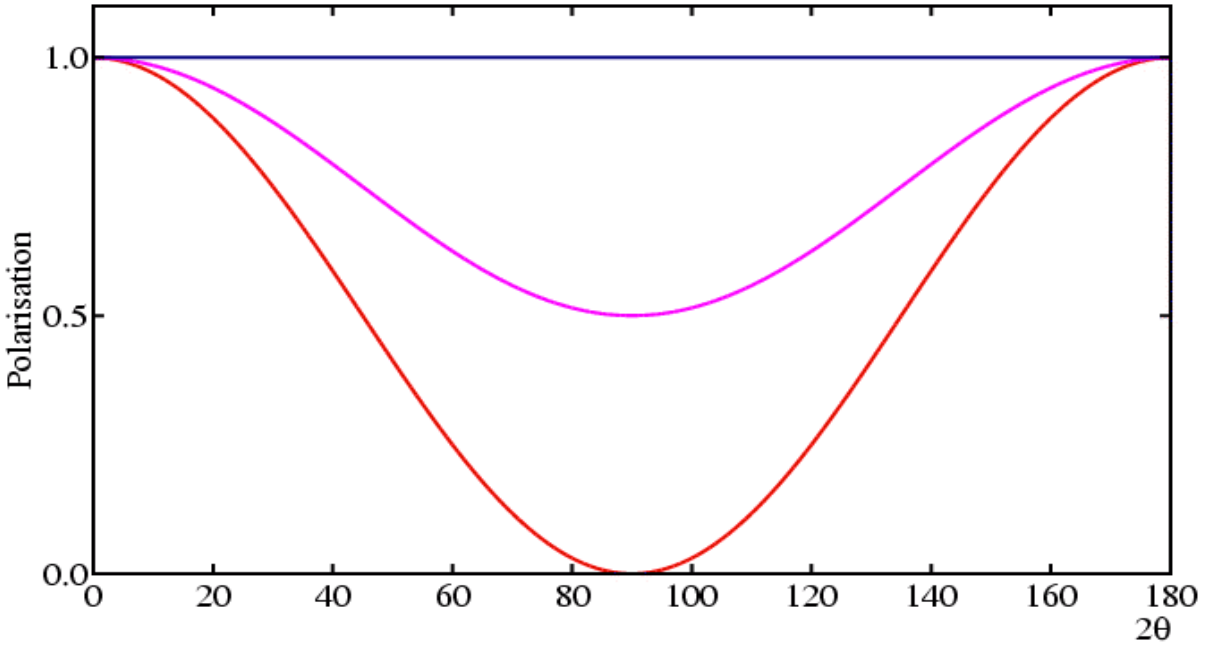

XMCD

Generace polarizovaného rtg záření

Difrakční křivka Si 004, Cu K alfa, 2theta=69.5 deg

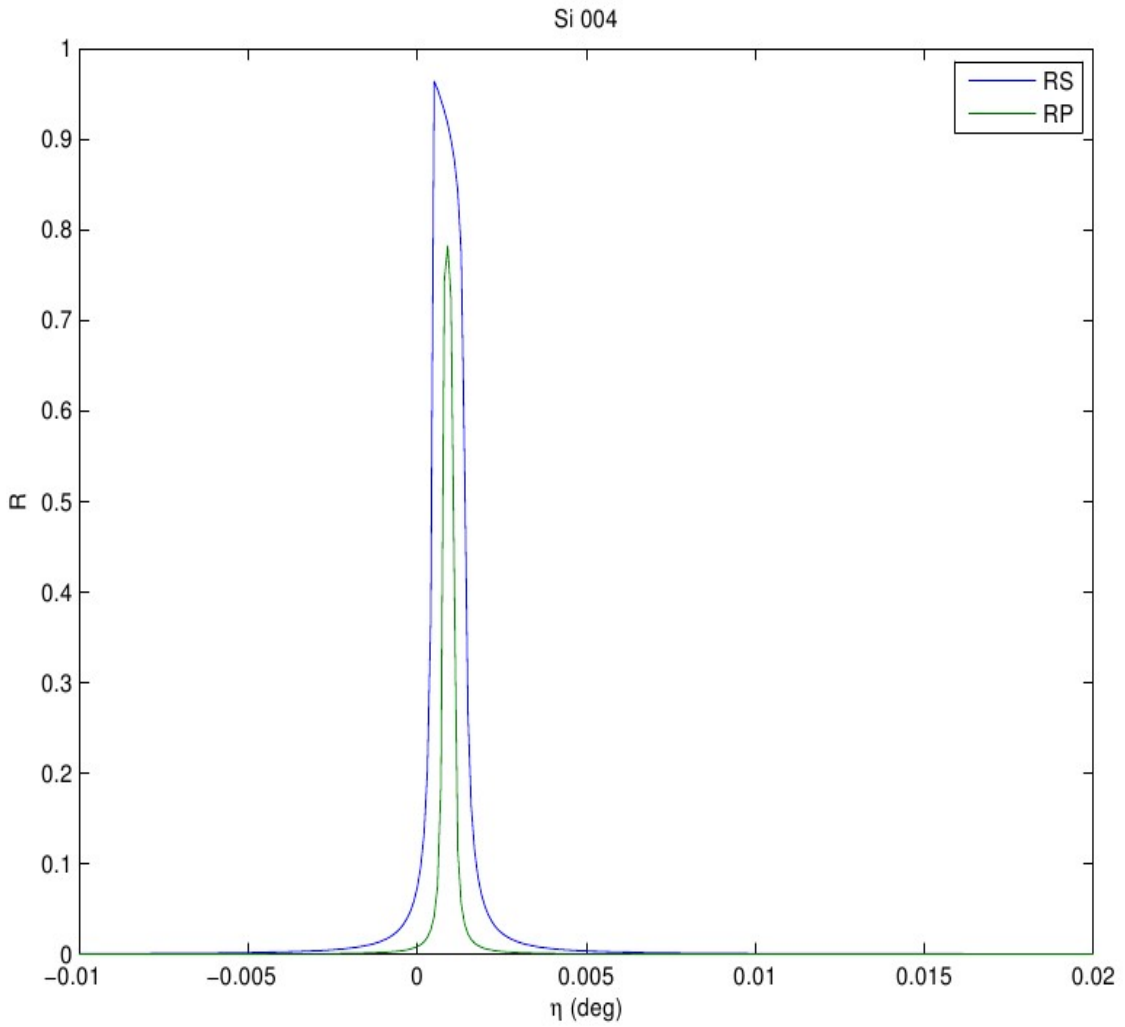

XMCD

Generace polarizovaného rtg záření

“čtvrtvlnná destička”

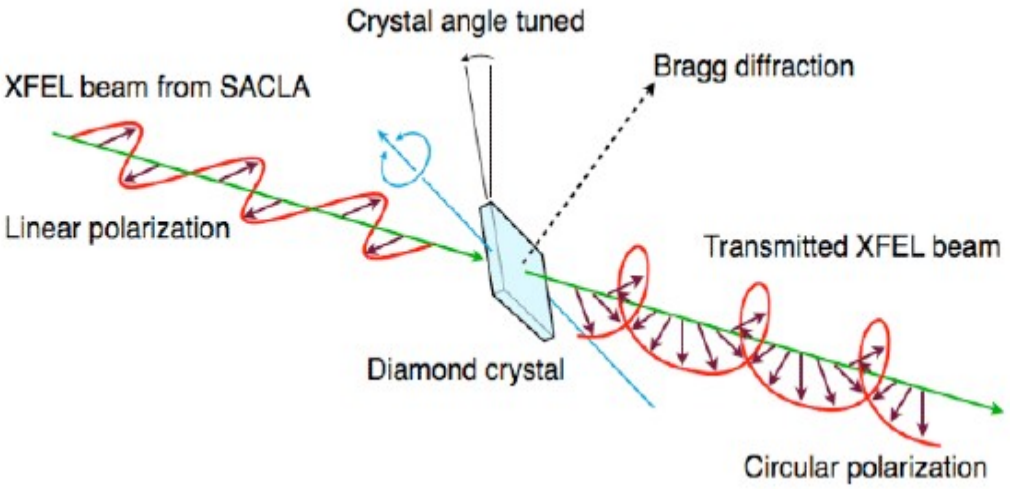

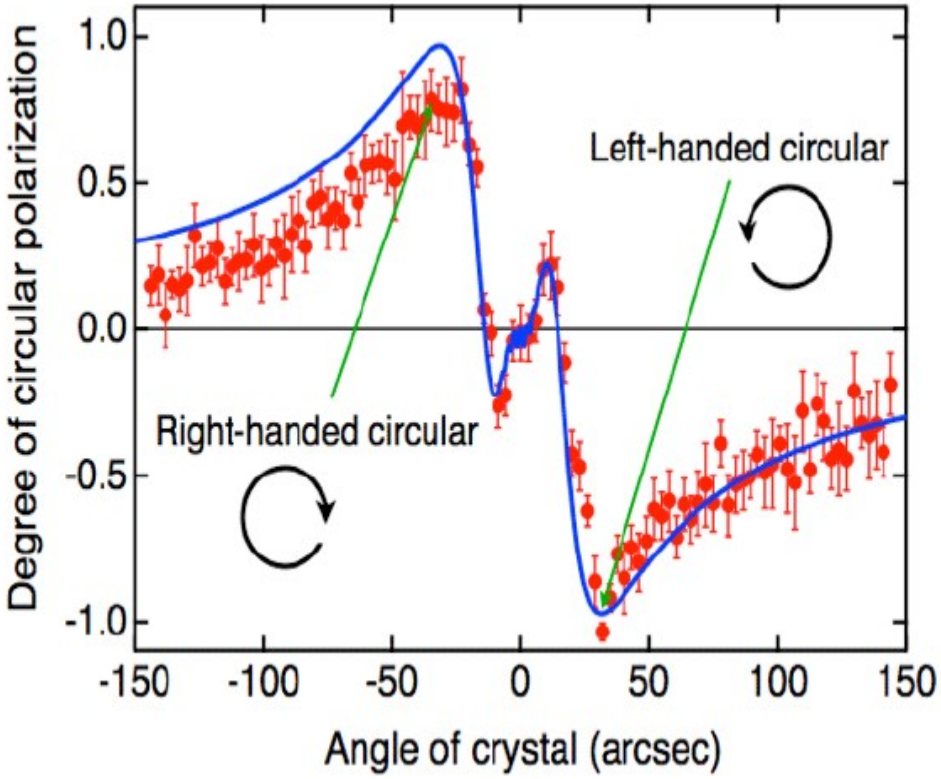

XMCD

PHYSICAL REVIEW B VOLUME 50, NUMBER 17 1 NOVEMBER 1994-I

Orbital and spin sum rules in x-ray magnetic circular dichroism

W. L. O'Brien
Synchrotron Radiation Center, University of Wisconsin–Madison, 3731 Schneider Drive, Stoughton, Wisconsin 53589

B. P. Tonner
Synchrotron Radiation Center, University of Wisconsin–Madison, 3731 Schneider Drive, Stoughton, Wisconsin 53589
and Department of Physics, University of Wisconsin–Milwaukee, 1900 East Kenwood Boulevard, Milwaukee, Wisconsin 53211
(Received 11 May 1994; revised manuscript received 5 July 1994)

Electron yield

$$Y_i(\hbar\omega) \propto \hbar\omega\sigma_i(\hbar\omega) ,$$

XMCD

$$\frac{\Delta A_{L_3}+\Delta A_{L_2}}{A_t}=\frac{\int_{L_3}\sigma_M(\hbar\omega)d\omega+\int_{L_2}\sigma_M(\hbar\omega)d\omega}{\int_{L_{2,3}}[\sigma_0(\hbar\omega)+\sigma_+(\hbar\omega)+\sigma_-(\hbar\omega)]d\omega}$$
$$=\frac{\langle L_z\rangle}{2n_h} \tag{8}$$

$$\frac{\Delta A_{L_3}-2\Delta A_{L_2}}{A_t}=\frac{\int_{L_3}\sigma_M(\hbar\omega)d\omega-2\int_{L_2}\sigma_M(\hbar\omega)d\omega}{\int_{L_{2,3}}[\sigma_0(\hbar\omega)+\sigma_+(\hbar\omega)+\sigma_-(\hbar\omega)]d\omega}$$
$$=\frac{2}{3n_h}\langle S_Z\rangle+\frac{7}{3n_h}\langle T_Z\rangle\ , \tag{9}$$

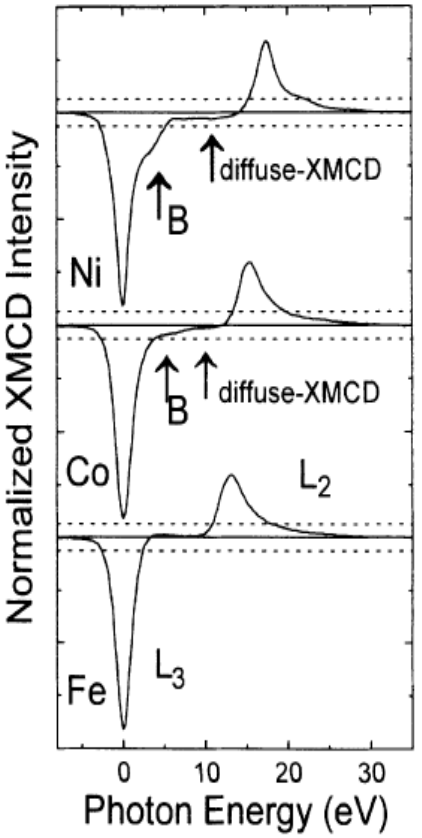

FIG. 6. Fe, Co, and Ni XMCD spectra shown normalized to constant L_3 peak height. The features labeled B are due to multiple initial-state configurations. The constant negative intensity between B and the L_2 peak in the Ni and Co spectra is due to diffuse magnetism.

XMCD

$$\langle L_z \rangle = -2n_h \cdot \frac{\int_{L_3+L_2}[I^{\uparrow\uparrow} - I^{\uparrow\downarrow}]d\omega}{\int_{L_3+L_2}[I^{\uparrow\uparrow} + I^0 + I^{\uparrow\downarrow}]d\omega}$$

$$\langle S_z \rangle = -\frac{3}{2} n_h \cdot \frac{\int_{L_3}[I^{\uparrow\uparrow} - I^{\uparrow\downarrow}]d\omega - 2\int_{L_2}[I^{\uparrow\uparrow} - I^{\uparrow\downarrow}]d\omega}{\int_{L_3+L_2}[I^{\uparrow\uparrow} + I^0 + I^{\uparrow\downarrow}]d\omega}$$

The final spectrum is the sum of 20 individual (F/I_0) sets for each side, with the X-ray photon angular momentum either parallel ($I^{\uparrow\uparrow}$) or antiparallel, ($I^{\uparrow\downarrow}$) to that of the C(II) majority 3d spin. Each of the averaged spectra were first normalized to

Here n_h represents the number of 3d vacancies in the metal ion, ω is the X-ray frequency, and I^0 refers to the absorption for X-rays linearly polarized along the magnetization direction; as is customary, we approximate this by $(I^{\uparrow\uparrow} + I^{\uparrow\downarrow})/2$. It is common in the XMCD literature[1,7,15] to refer to the first integral in the numerator of eq 2 as "A", the second integral as "B", and the denominator as "$3C$". The necessary integrals are illustrated in Figure 1. One can thus re-express the sum rules in the following manner, in units of $\hbar$/atom:

$$\langle L_z \rangle = -n_h \frac{2(A+B)}{3C} \qquad \langle S_z \rangle = -n_h \frac{A-2B}{2C} \qquad (3)$$

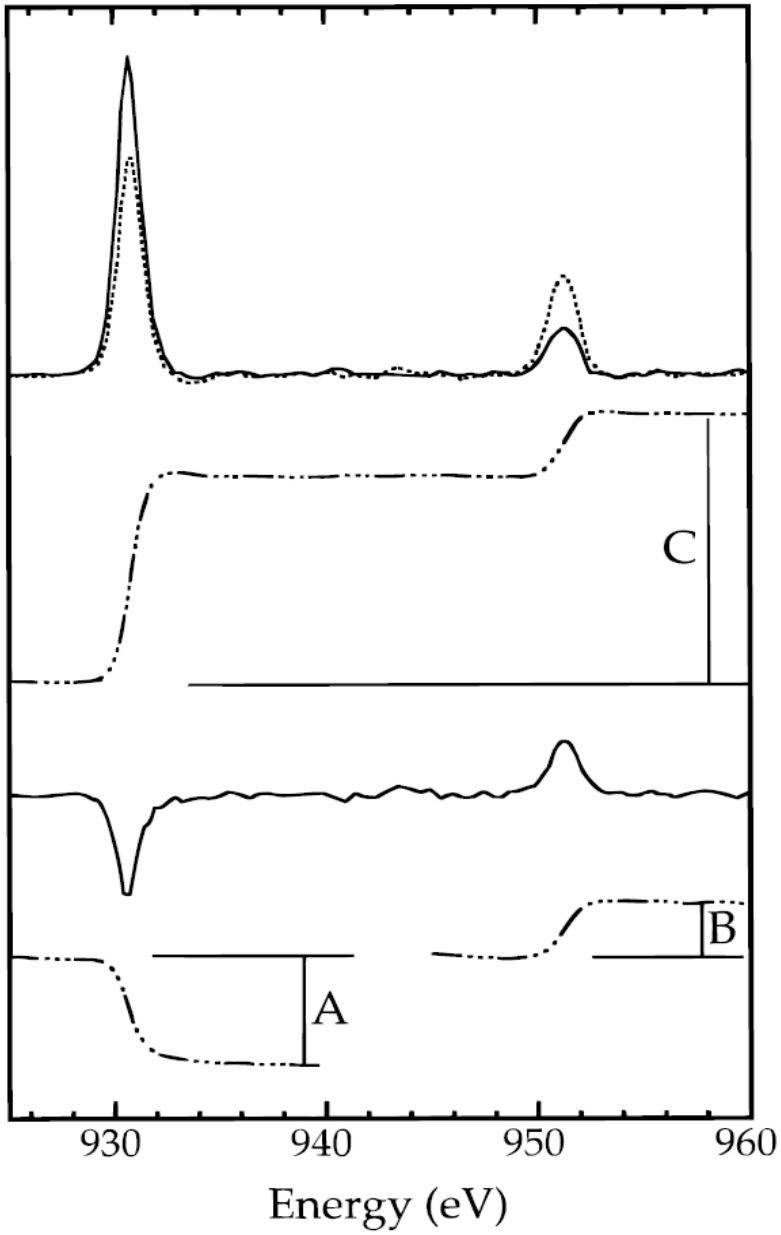

XMCD Mn in Bi2Se3

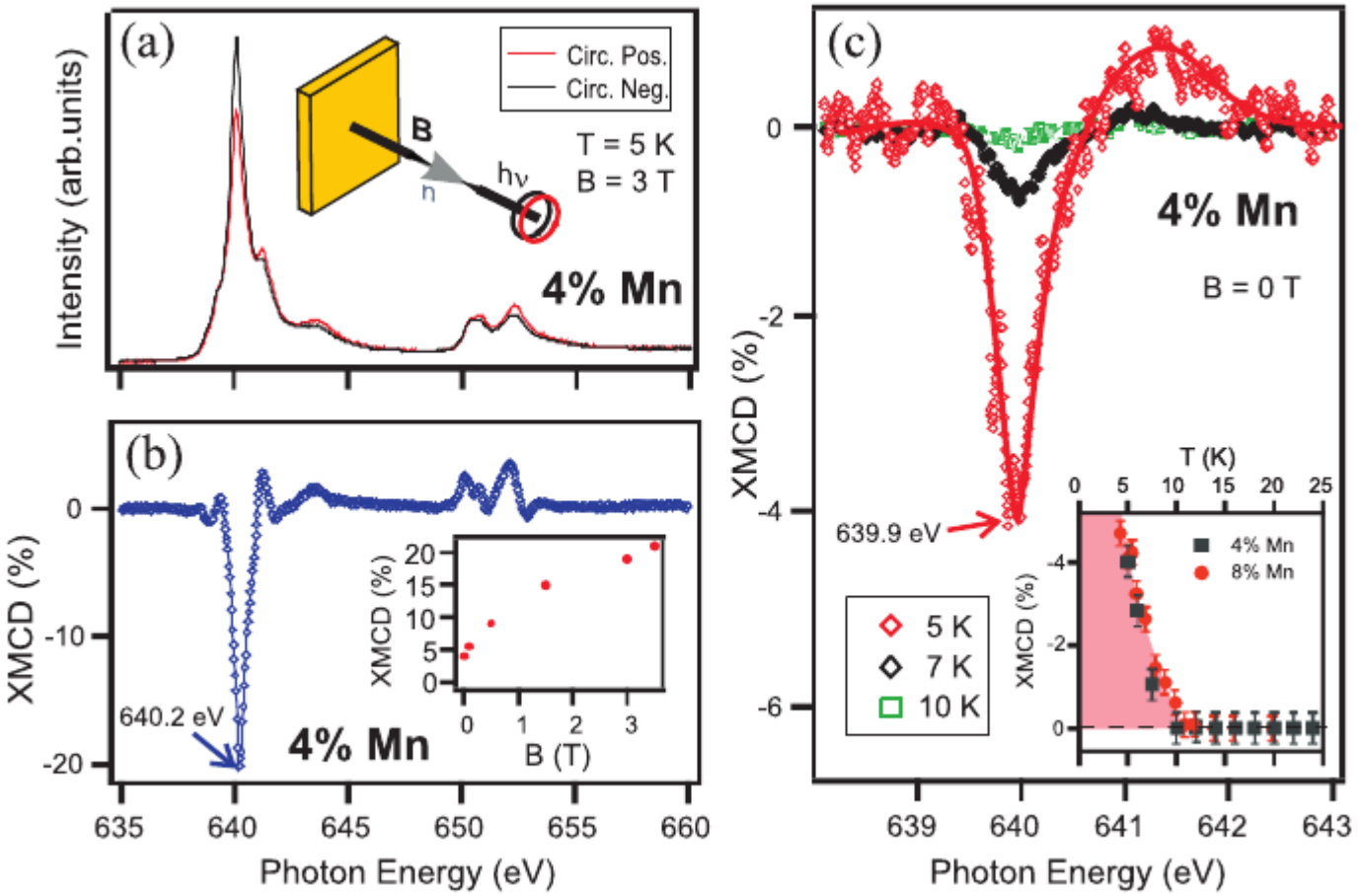

FIG. 4. (Color online) XMCD in total electron yield at the Mn $L_{2,3}$-edges. (a) X-ray aborption spectra measured for opposite helicities of the circularly polarized incident light at 5 K with a out-of-plane applied magnetic field of 3 T. A sketch of the experimental geometry is also shown. (b) Corresponding XMCD difference spectrum. The inset shows XMCD measurements for different applied magnetic fields. (c) Temperature dependence of the remanent XMCD for a Mn concentration of $x = 0.04$. Inset: Detailed temperature dependence for various Mn concentrations.

XMCD

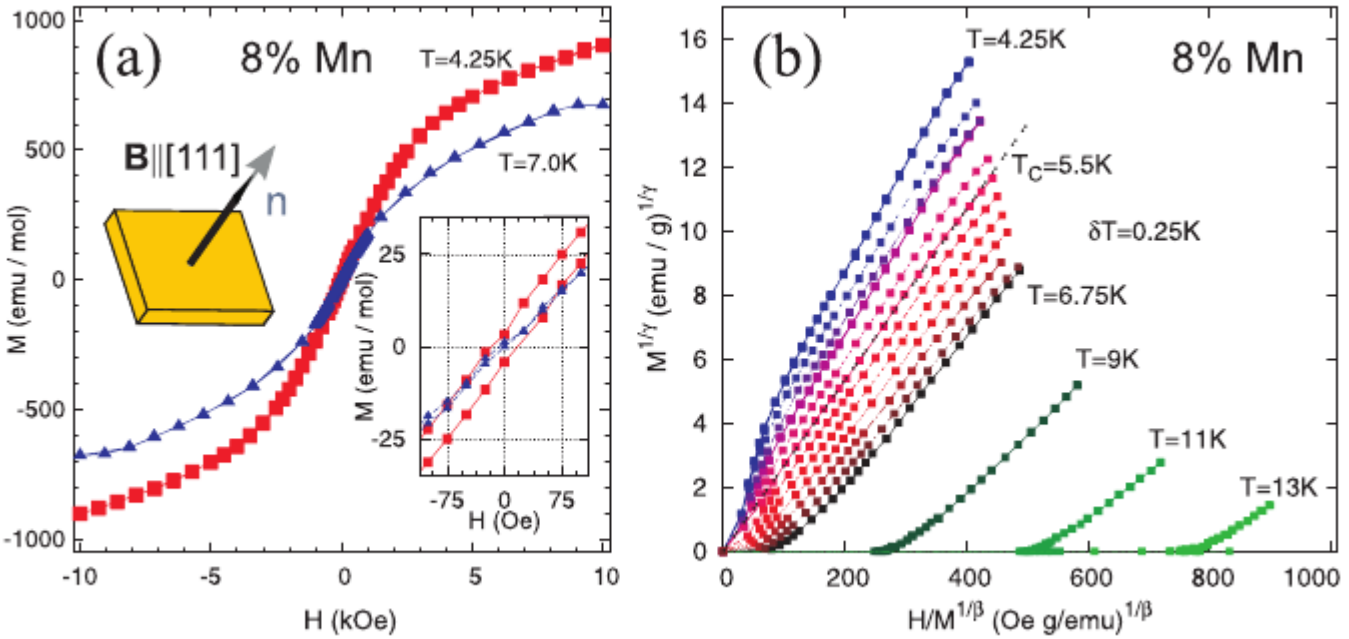

FIG. 3. (Color online) (a) Hysteresis loops measured at a temperature of 4.2 K (squares) and 7 K (triangles), respectively. The applied magnetic field is perpendicular to the (111) sample surface (see sketch). Inset: A zoom-in around zero magnetic field showing hysteresis at 4.2 K and a paramagnetic state at 7 K. (b) Modified normalized Arrott plots at various temperatures from which a Curie temperature of 5.5 K is deduced. Between 4.25 and 6.75 K, data are shown for increments of $\delta T = 0.25$ K.

RIXS

Rezonanční neelastický rtg rozptyl – rezonanční “Ramanův” rozptyl
Výhoda Rtg proti VIS – směrové rozlišení, možnost pokrytí celé Brillouinovy zóny
Nevýhoda – slabší jevy, experimentální obtížnost energiového rozlišení

Rezonance –
Silné zesílení jevu

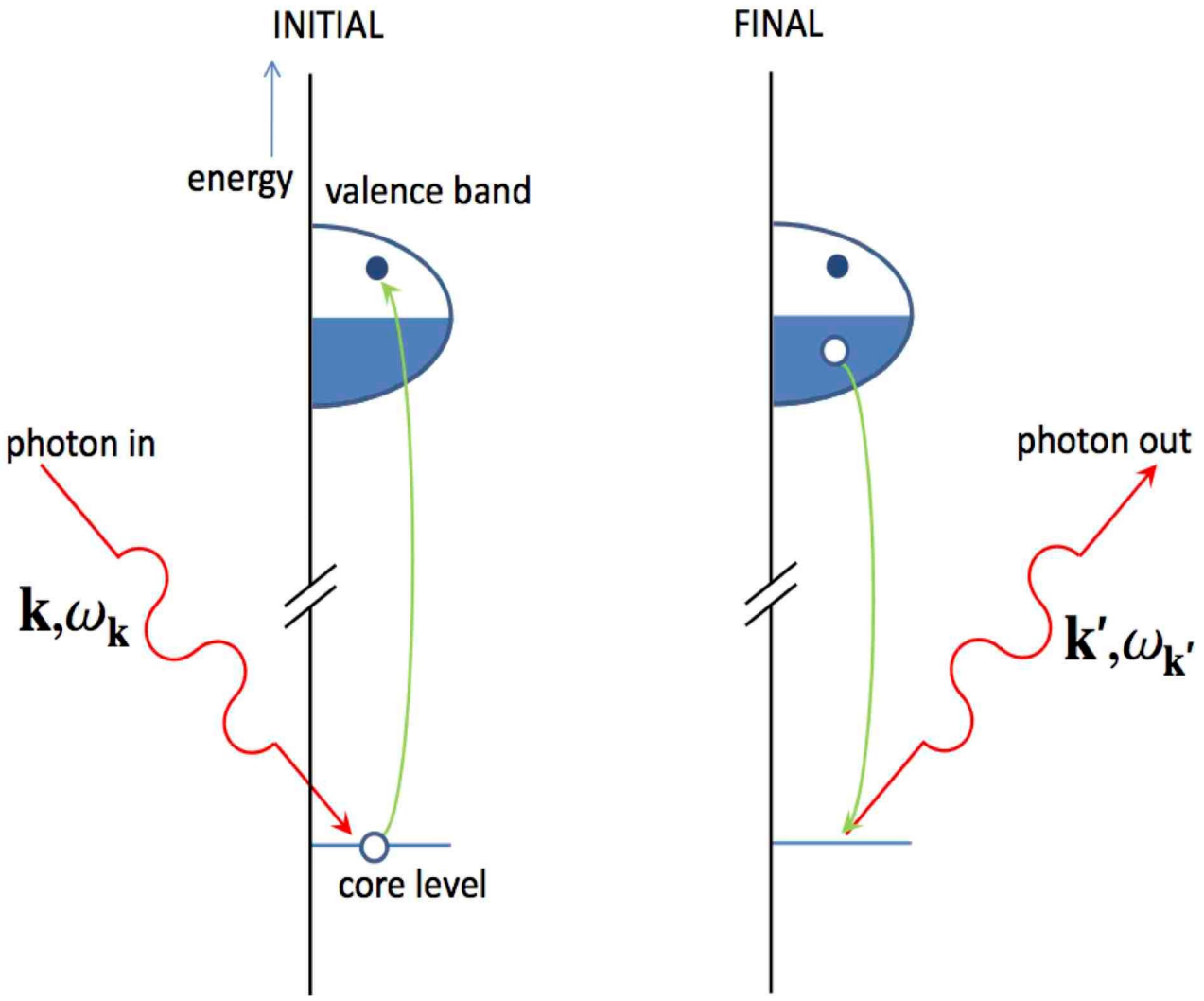

RIXS

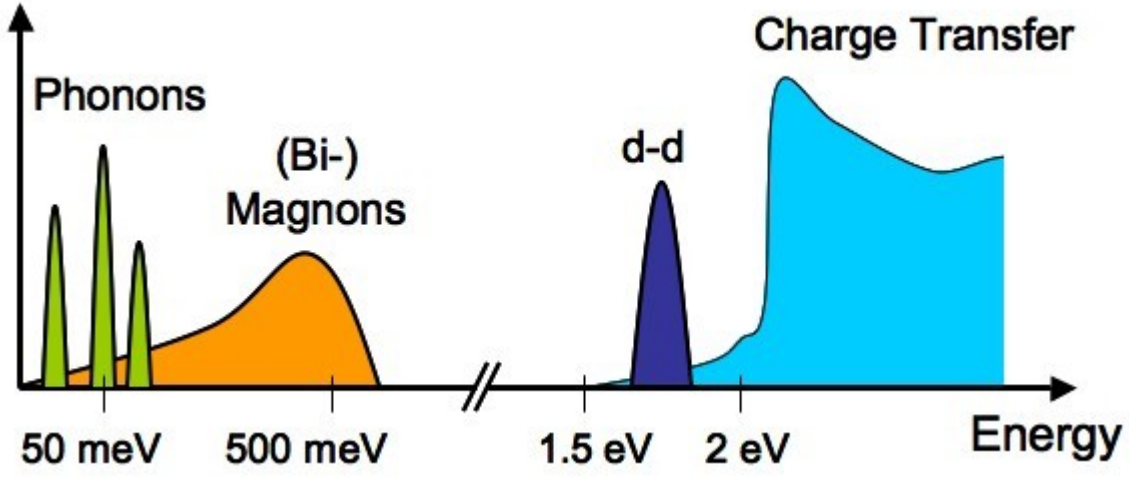

Elementary excitations in condensed matter systems that can be measured by RIXS. The indicated energy scales are the ones relevant for transition metal oxides.

RIXS

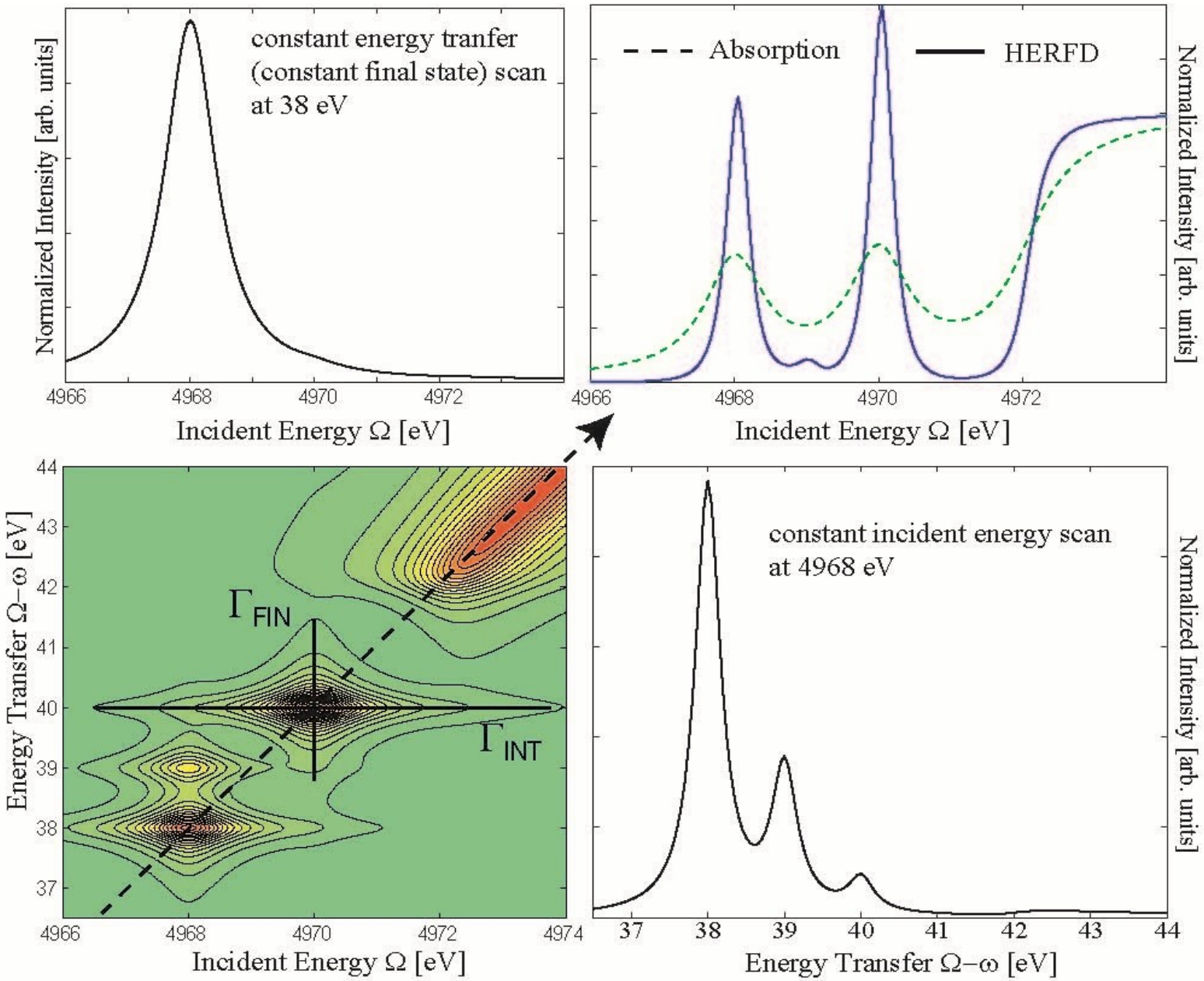
constant energy tranfer
(constant final state) scan
at 38 eV
Normalized Intensity [arb. units]
Incident Energy Ω [eV]
Absorption
HERFD
Normalized Intensity [arb. units]
Incident Energy Ω [eV]
Energy Transfer Ω−ω [eV]
Γ FIN
Γ INT
Incident Energy Ω [eV]
constant incident energy scan
at 4968 eV
Normalized Intensity [arb. units]
Energy Transfer Ω−ω [eV]

RIXS

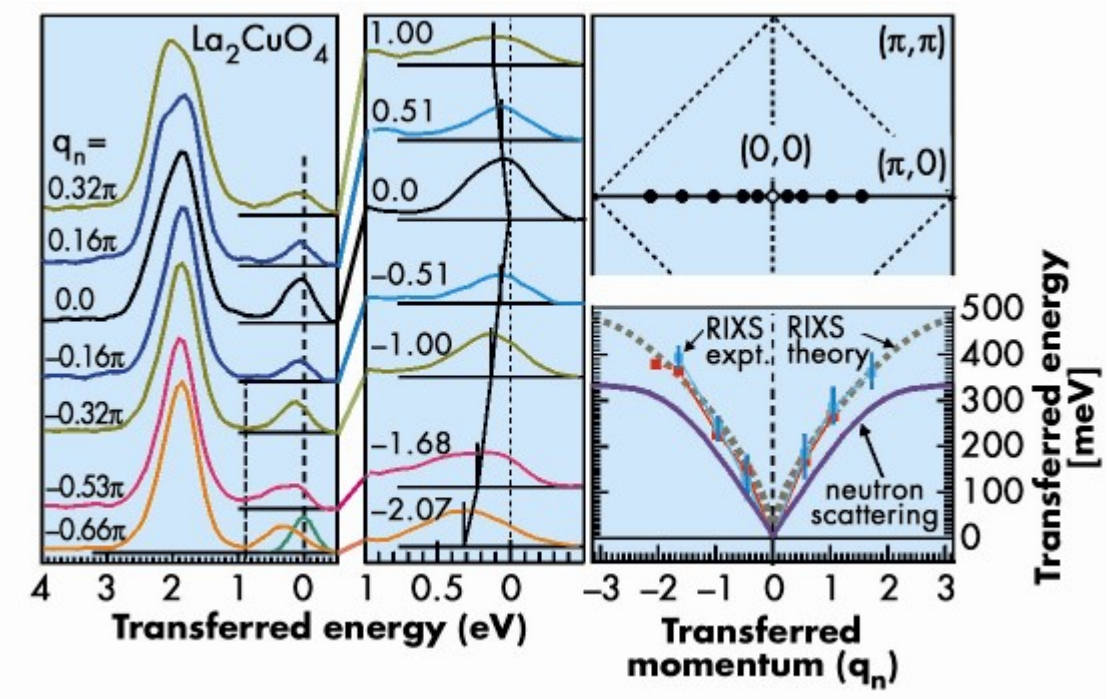

Cu L3 RIXS results of La2CuO4. The peak dispersion curve was extracted from the raw data (left panel) corresponding to the given dots in the Brillouin zone.

L. Braicovich (a), L.J.P. Ament (b), V. Bisogni (c), F. Forte (b,d), C. Aruta (e), G. Balestrino (f), N.B. Brookes (c), G.M. De Luca (e), P.G. Medaglia (f), F. Miletto Granozio (e), M. Radovic (e), M. Salluzzo (e), J. van den Brink (b,g), and G. Ghiringhelli (a), arXiv:0807:1140v1, (2008).

RIXS

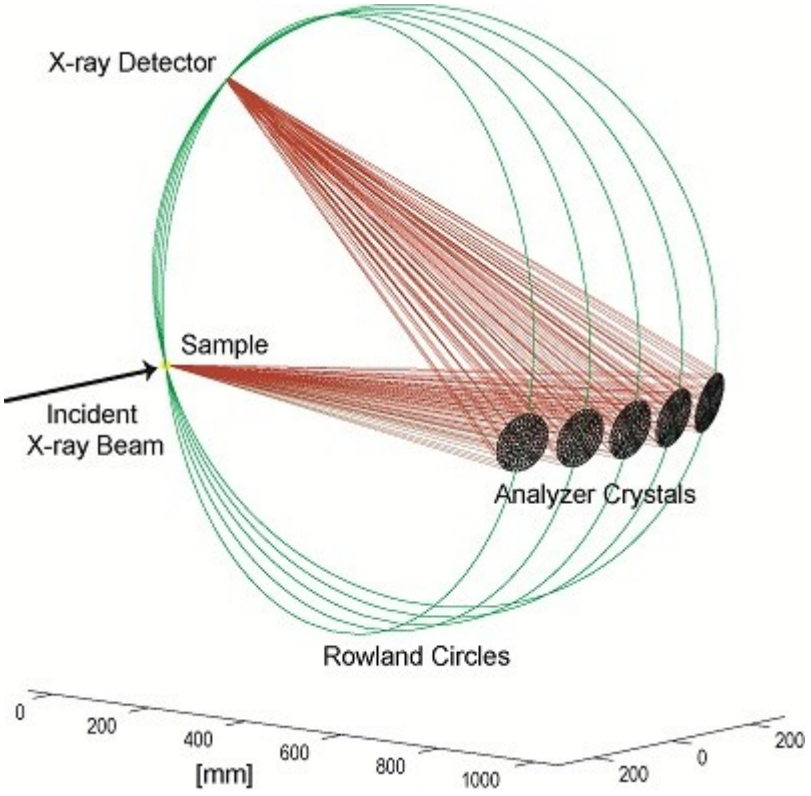

$$F(\Omega,\omega)=\sum_f\left|\sum_n\frac{\langle f|T_2|n\rangle\langle n|T_1|g\rangle}{E_g-E_n+\Omega-i\frac{\Gamma_{INT}}{2}}\right|^2 * \frac{\frac{\Gamma_{FIN}}{2\pi}}{(E_g-E_f+\Omega-\omega)^2+\frac{\Gamma_{FIN}^2}{4}}$$

RIXS

ESRF

A high resolution soft X-ray RIXS spectrometer reaching a combined resolving power E/ΔE better than 30,000. The spectrometer features an 11m long scattering arm capable of rotating over 100º without breaking vacuum, and a full in-vacuum 4-circle sample goniometer. The instrument was designed and developed in collaboration with Giacomo Ghiringhelli & Lucio Braicovich from Politecnico di Milano.

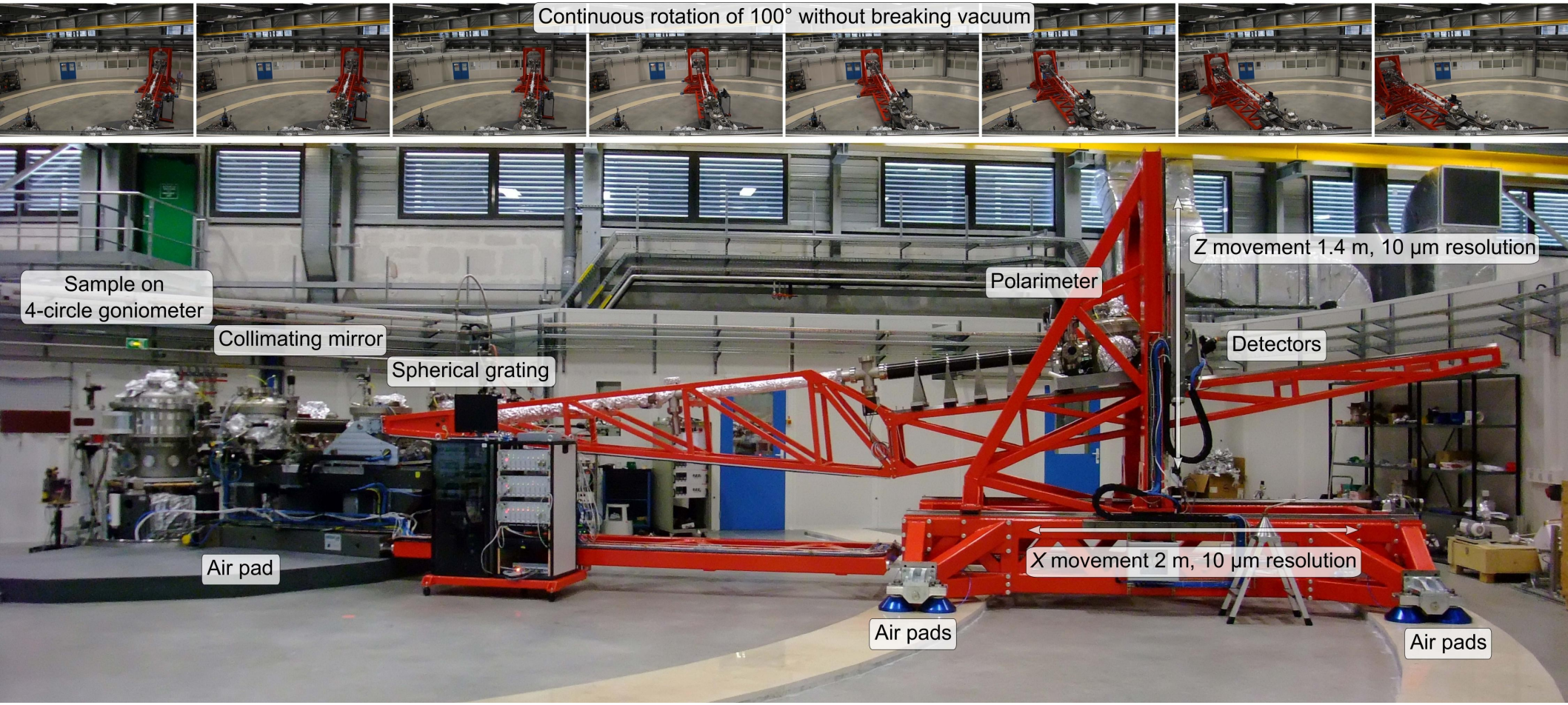

RIXS

ESRF

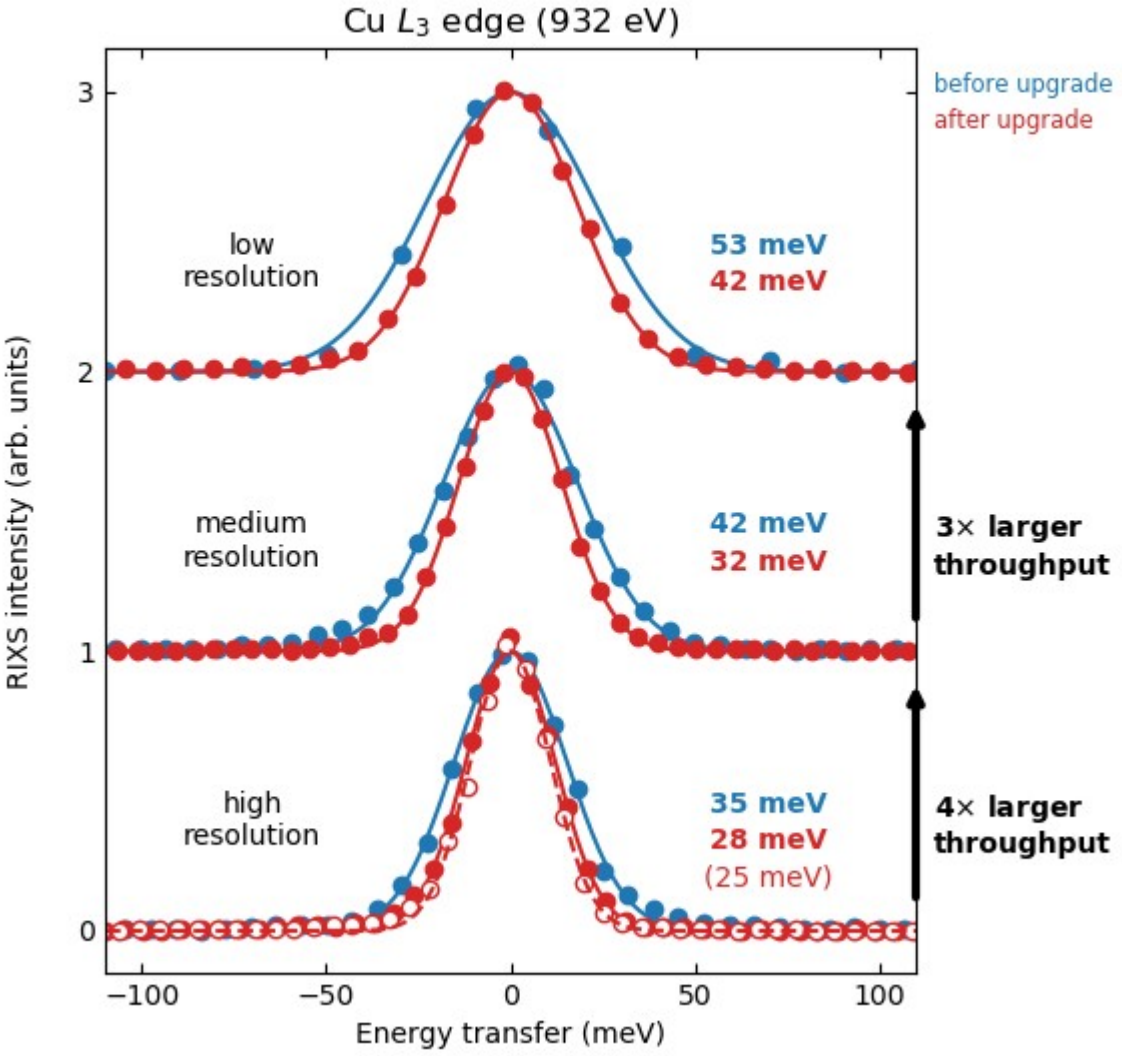
Cu L_3 edge (932 eV)
RIXS intensity (arb. units)
Energy transfer (meV)
before upgrade
after upgrade
low resolution
53 meV
42 meV
medium resolution
42 meV
32 meV
high resolution
35 meV
28 meV
(25 meV)
3× larger throughput
4× larger throughput

Bodové rtg detektory

- Ionizační
- Geiger-Müller – vysoké napětí, Townsendova lavina
- Proporcionální – nižší napětí, rozlišení > 20 % (> 10^3 eV)

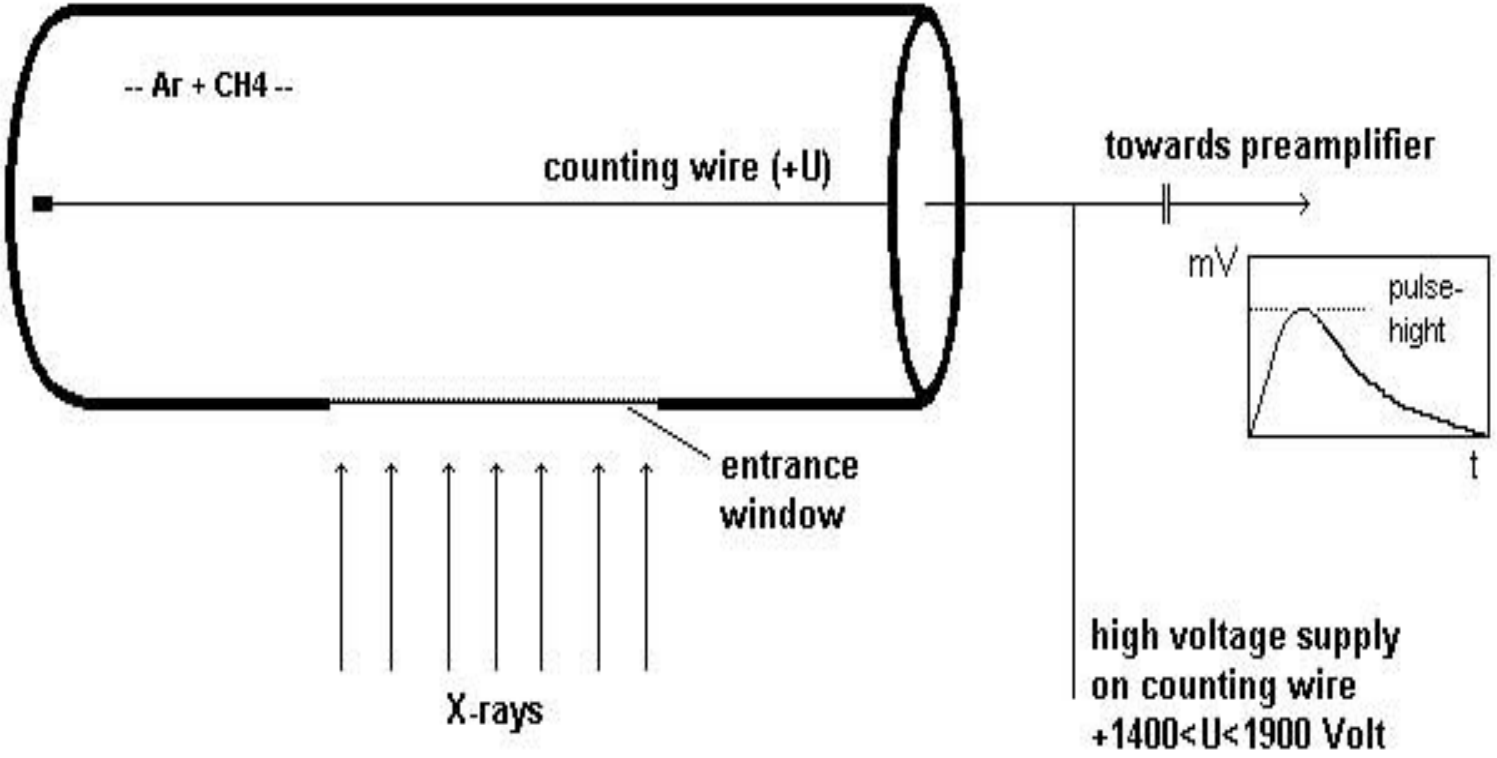

Bodové rtg detektory

- Scintilační – rozlišení 5 až 10 % (10^3 eV)
  NaI(Tl) – od 6keV účinnost téměř 100%
  Emise 410 nm – 3eV

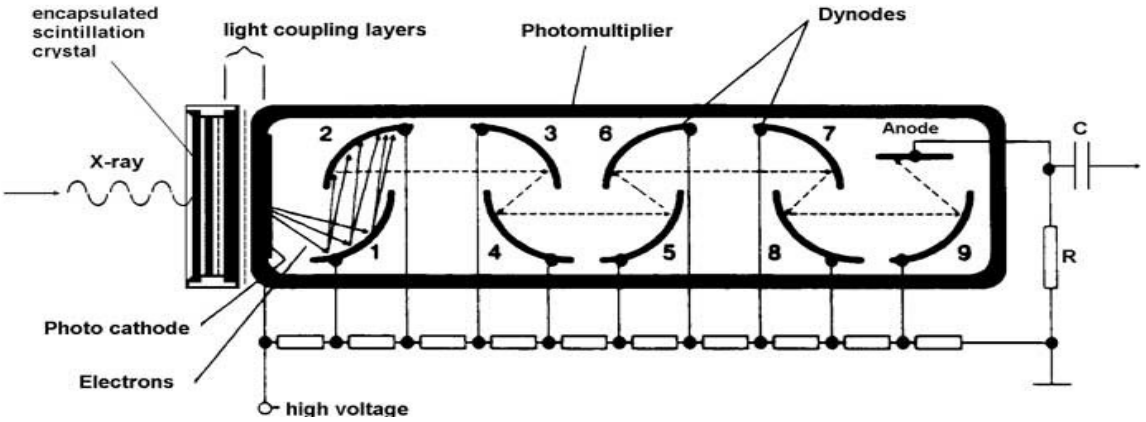

- Polovodičové
  – rozlišení až 2 % (10^1 - 10^2 eV)

Si, Ge

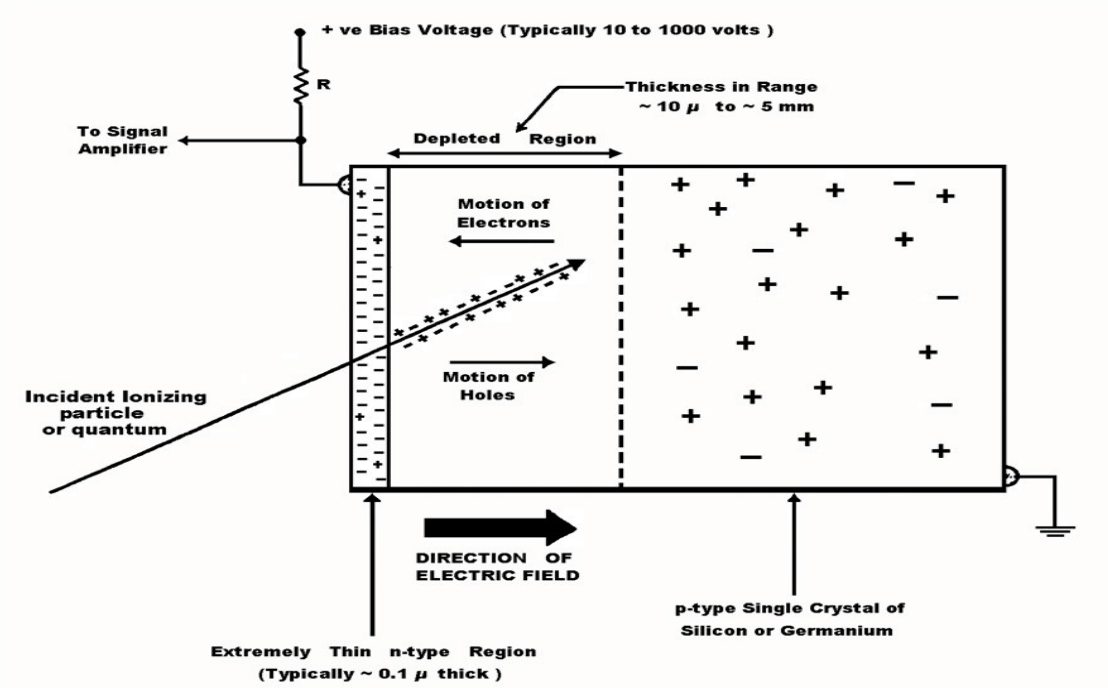

Polovodičové rtg detektory

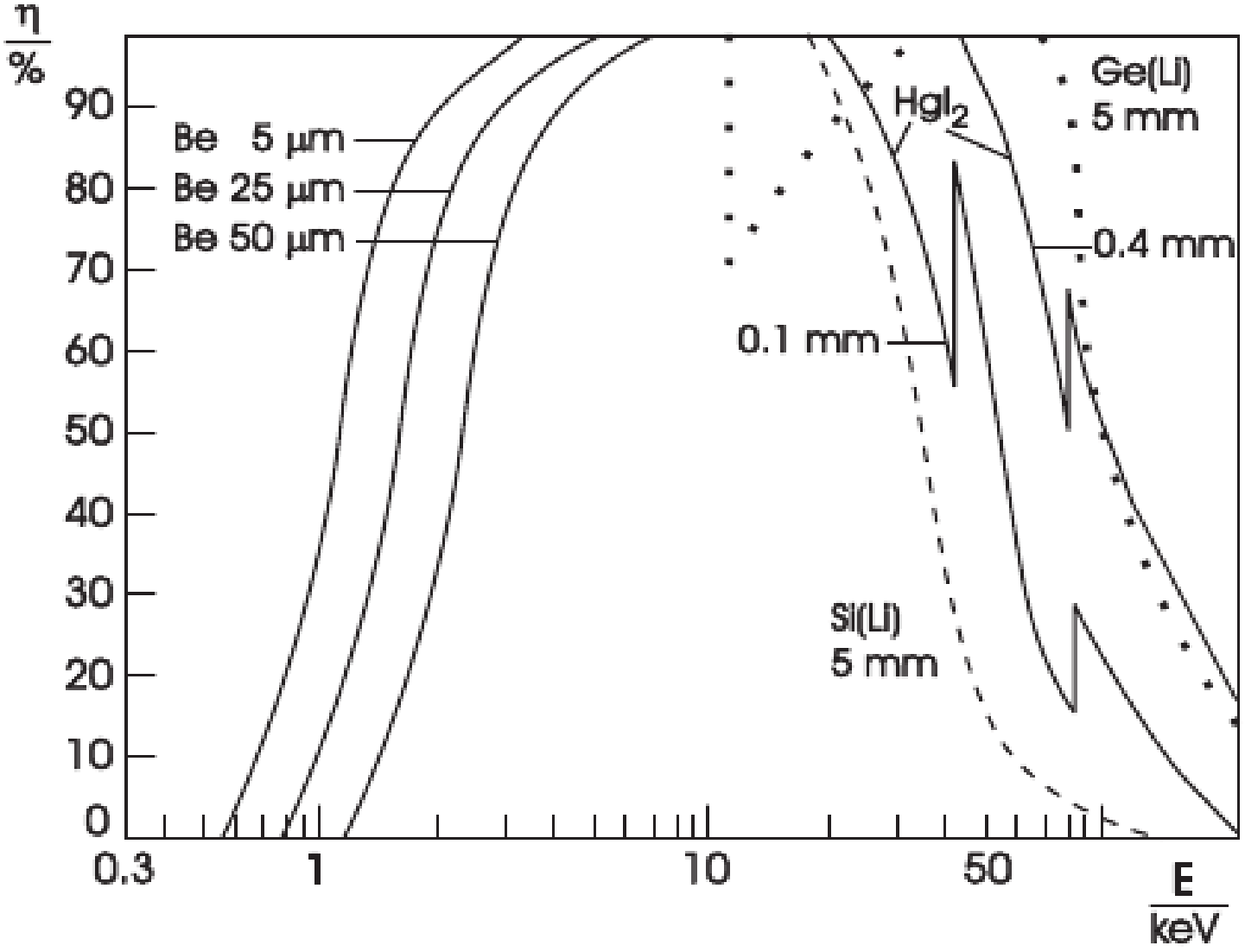

Lineární rtg detektory

- Plynové – ionizační, malý dynamický rozsah (50 kcps),
- Polovodičové – velký dynamický rozsah

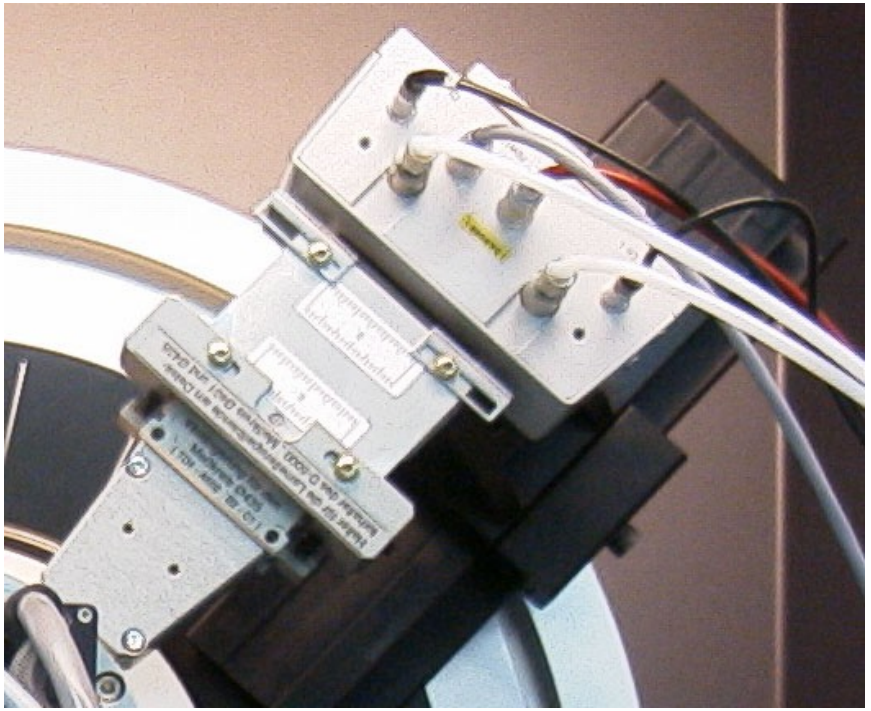

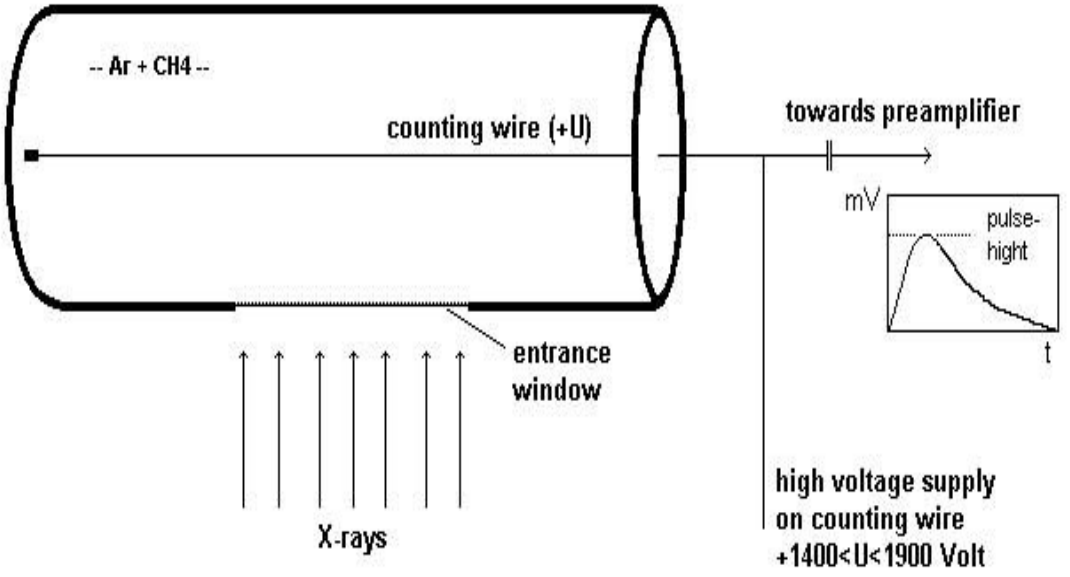

Plošné rtg detektory

- Plynové - ionizační
- CCD - rozlišení cca $(50\mu m)^2$
- Film - rozlišení cca $(1\mu m)^2$, nelineární, velmi pomalé
- Luminiscenční (“Image plate”) - rozlišení cca $(10\mu m)^2$, velké plochy

rychlost 1 snímek cca 3 až 10 minut.

- Scintilační - rozlišení až cca $(3\mu m)^2$, malá kvantová výtěžnost (tenký scintilátor)
- Polovodičové

Rtg detektory

Table 4-2. *Properties of common x-ray detectors; ΔE is measured as FWHM.*

Detector	Energy range (keV)	$\Delta E/E$ at 5.9 keV (%)	Dead time/event (μs)	Maximum count rate (s^{-1})
Gas ionization (current mode)	0.2–50	n/a	n/a	10^{11}[a]
Gas proportional	0.2–50	15	0.2	10^6
Multiwire and microstrip proportional	3–50	20	0.2	$10^6/mm^2$
Scintillation [NaI(Tl)]	3–10,000	40	0.25	2×10^6
Energy-resolving semiconductor	1–10,000	3	0.5–30	2×10^5
Surface-barrier (current mode)	0.1–20	n/a	n/a	10^8
Avalanche photodiode	0.1–50	20	0.001	10^8
CCD	0.1–70	n/a	n/a	n/a
Superconducting	0.1–4	< 0.5	100	5×10^3
Image plate	4–80	n/a	n/a	n/a

[a] Maximum count rate is limited by space-charge effects to around 10^{11} photons/s per cm^3.